MICROSTRUCTURAL ENGINEERING AND THERMOELECTRIC PROPERTIES OF PSEUDO-BINARY Sn-Bi-Te SYSTEMS

Thesis Submitted for the Degree of

M.Sc.

By

Endale Abebe Gudeta

Supervisor: Dr. Olu Emanuel Femi (PhD)

Faculty of Materials Science and Engineering

Jimma Institute of Technology

Jimma University

November 30, 2018

To
The Glory of God

Declaration

All the contents of this research were conducted by the author, Endale Abebe Gudeta, with the supervision of Dr. Olu Emanuel Femi. I had performed the practical experiments mentioned in this research under the supervision of Prof. Kamanio Chattopadhyay. The experimental part of this research had been conducted in the Department of Materials Engineering, Indian Institute of Science, IISc, Bangalore, India, under the supervision of Prof. Kamanio Chattopadhyay. Based on this work I have written this thesis and related works. This thesis is expected to satisfy the partial fulfillment for M.Sc. degree in Materials Science and Engineering.

To the best of the author, this work has not been used for the award of any degree or diploma, but I would like to extend my heartfelt gratitude for the researchers whose work that has been referred in my thesis, and I deeply regretted any error that occurs while referring to others work.

Endale Abebe Gudeta

November 30, 2018

JIMMA UNIVERSITY

JIMMA INSTITUTE OF TECHNOLOGY

FACULTY OF MATERIALS SCIENCE AND ENGINEERING

Master's Thesis on

Microstructural Engineering and Thermoelectric Properties of Pseudo-Binary Sn-Bi-Te Systems

By Endale Abebe Gudeta

Approved by Board of Examiners

1.	_____	_____	___/___/___
	External Examiner	Signature	Date
2.	_____	_____	___/___/___
	Internal Examiner	Signature	Date
3.	_____	_____	___/___/___
	Chairperson of the Board	Signature	Date
4.	_____	_____	___/___/___
	Advisor	Signature	Date

Acknowledgments

My heartfelt gratitude goes to my supervisor Dr. Olu Emanuel Femi, who had introduced this field for me; enables me to identify the problem investigated in this work and to get lab facility, and was willing to supervise me until this work was finalized.

The author wants to extend his thanks to Prof. Kamanio Chattopadhyay, for giving the opportunity to work in his laboratory.

I would like to appreciate the collaboration between Indian Institute of Science, IISc, and Jimma Institute of Technology, JIT, which gives the opportunity to use the lab facility of IISc for JIT staffs including the author.

I have sincerely acknowledged the students of Prof. Kamanio Chattopadhyay for their continuous help during the experimental work that enables the author to learn not only the experimental work and the data analyzing techniques but also team spirit, cooperation, hard work etcetera.

Abstract

The growing demand for energy needs better materials for energy conversion. One class of materials to address the problem are materials for conversion of waste heat to electricity, which are called thermoelectric materials. Even though SnTe and Bi_2Te_3 are important thermoelectric materials, the phase diagram and microstructural studies of their pseudo-binary system are not well investigated. Since these microstructures can determine the property of the material, investigation of the relationship between microstructure and thermoelectric property of Sn-Bi-Te system is anticipated to result in the finding of new thermoelectric material. Therefore, this research is aimed to study the variation of microstructures with the composition of selected samples. The thermoelectric properties have been investigated as a function of variation in microstructures.

This research contains two parts. The first part aims at determining the effect of Bi addition to the SnTe system. It includes investigation of the microstructural, mechanical and thermoelectric properties of the system. This work describes the nature of the microstructure of the system. The study of the mechanical property concerns the change of Vickers hardness with aging heat treatment. The study of the thermoelectric properties was as a function of both composition and temperature. This group samples had created small SnTe phases compacted with Bi. Such a structure has a high probability of scattering phonon while allowing electrical conduction and hence enables the high value of the Seebeck coefficient.

The second part considers a group of samples which were studied to investigate the relatively complex nature microstructure of the SnTe - Bi_2Te_3 system. It focuses on the region where Bi_2Te_3 is soluble in SnTe. Both composition and processing methods result in the creation of different kind of microstructures. The study of the microstructure in this region focuses on determining the phases and crystal structure of the system. This part of the research aims at exploring different compositions which have a high potential for thermoelectric application.

Key words: thermoelectric, pseudo-binary, Seebeck effect, Bi-Sn-Te system, heat treatment,

Glossary

XRD – X-ray Diffraction

SEM – Scanning Electron Microscopy

EPMA – Electron Probe Microanalyzer

EDS – Energy Dispersive Spectroscopy

WDS – Wavelength Dispersive Spectroscopy

χ^2 – Goodness of Fit

α – Seebeck Coefficient

σ – Electrical conductivity

ρ – Electrical Resistivity

κ – Total thermal conductivity

κ_e – Electronic Thermal conductivity

κ_l/ κ_p – Lattice/ Phonon thermal conductivity

$\alpha^2\sigma$ – Power Factor

ZT – Dimensionless Figure of Merit

T – Temperature

H – Hot

C – Cold

η – Efficiency of thermoelectric device

L – Lorentz number

GoF – Goodness of fit

SOF – site occupancy factore

Contents

CHAPTER 1

LITERATURE REVIEW

1.1 Introduction

The modern world is almost totally dependent on energy consuming manufacturing industries. These industries are vulnerable for unnecessary energy waste, out of the limited energy supply, in the form of heat. This is observed in many industries, for instance in cement producing industries; and in iron extraction and steel processing plant. The wastage of energy in the form of heat creates not only an energy shortage but also causes environmental pollution on the glowing planet, earth. Discovering an efficient material that can be fixed at the exhaust of the waste heat and can absorb the heat energy to convert it to electrical energy is one way of solving both of the above problems. Such kind of material can be explained by similar analogy with Compton Effect, where the applied energy to a material exits electrons from the material provided that the applied energy is greater than the energy band gap of the material; except the fact that Compton Effect is usually related with light energy, instead of heat energy. These materials are mainly semiconductors, specifically called thermoelectric materials.

Recycling of waste heat is one way of providing energy supply for the continuously growing demand. This requires an efficient conversion of waste heat to electricity. On the other hand, some equipment, for instance, refrigerator and heating staffs, need an efficient conversion of electric energy to heat energy or cooling. The conversion of heat energy to electricity is due to the Seebeck effect [1] while the reverse process depends on the Pietler effect [1-3]. These are typical thermoelectric effects which enable energy conversion. These thermoelectric properties are usually observed on both organic and inorganic materials. Bi_2Te_3, $CoSb_3$, Cu_2Se, SnSe, SnTe, PbTe and

SiGe are typical inorganic thermoelectric materials [4, 5]. Many polymers are also known for thermoelectric applications [6]. Polyacetylene (PAC), polypyrrole (PPY), polythiophene (PT), polyaniline (PANI), poly (p-phenylene vinylene) (PPV), poly(p-phenylene) (PPP), and their derivatives [7] are typical thermoelectric materials.

Since these materials are used under the application of heat energy, the range of temperature through which the material maintains its thermal stability is an important parameter. Various sources of waste heat have a different range of temperature. Therefore thermoelectric materials can be categorized under the different range of temperatures for practical application. A rough classification is low-temperature; medium-temperature; and high-temperature applications. The corresponding power sources are low-grade, medium-grade and high-grade power sources [8]. The classification based on temperature consists of high-grade (500 – 1500 ″C), medium-grade (250 – 500 ″C) and low-grade (40 – 250 ″C) [7].

This chapter describes the general feature, working mechanism, improvement techniques, and Nobel achievements by different researchers on thermoelectric materials. The methodologies, instruments, techniques, and processes used in this work are described in chapter two. The practical experiments conducted in this work are classified into two groups and presented in chapter three and chapter four. The final chapter provides a summary of all activities included in this work; some limitations of the work; recommendations for those who like to study this field; and potential future works.

1.2 The Origin of Thermoelectrics

The origin of thermoelectric properties is believed to be in 1821 when T.J. Seebeck found the generation of electricity by applying heat energy to a thermocouple. This is called the Seebeck

effect [9]. The original experiment was conducted on metallic conductors rather than on semiconductor material. The Seebeck effect was shown at the junction of the conductors. As shown in figure 1.1, providing heat energy to the junction results in the detection of potential difference by the galvanometer. On the other hand, replacing the galvanometer by electric source produces a change in temperature at the junction. This is another phenomenon called Peitier effect, after J. Peltier, in 1834 [9]. In fact, these two effects are not independent of each other. The interdependency is discovered by W. Thomson (who later became Lord Kelvin) in 1855 [9]. This discovery is explained by Thomson's coefficient.

The reason behind the observed potential difference after heating the interface, shown in figure 1.1, was initially thought to be as an interfacial property. But later on, it has been understood that it is the result of the thermodynamic temperature difference between the two ends of one of the conductors that results in the creation of the potential difference [9]. The heat energy absorbed from the source will increase the kinetic energy of the charge carriers of the two dissimilar conductors, so that the temperature difference between the ends of each of the conductor will result in the creation of potential gradient with opposite polarity that has been detected by the galvanometer.

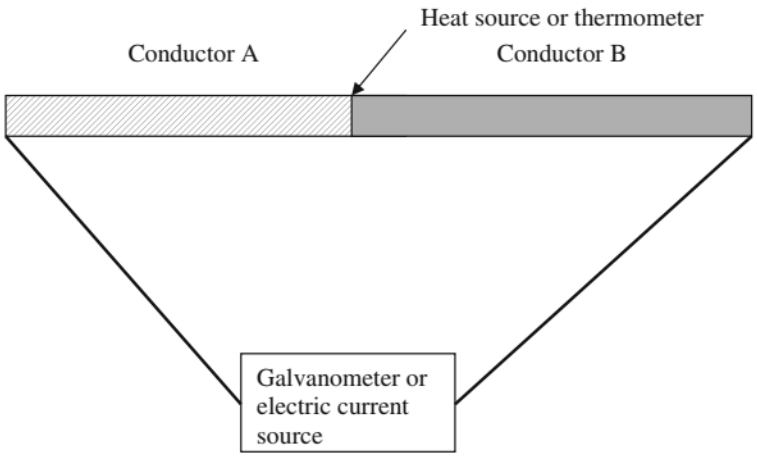

Figure 1.1: Experiment to demonstrate the Seebeck and Peltier effects [9].

These effects and the associated coefficients are explained by simple thermocouple as shown in figure 1.2. Two junctions are established between the two thermocouples while breaking thermocouple B. The broken ends of thermocouple B are used to be in contact with the galvanometer, or electric current source. When heat energy is applied to one of the junctions there will be a temperature gradient between the two junctions and associated potential difference. Hence, the Seebeck coefficient, α, is defined as the ratio of the change in potential difference to the temperature gradient, as shown by equation 1.1. If current source is connected at the junction instead of the galvanometer, and one of the junction is produced heat while the other gets cooled, this will be explained by the Peltier effect. Therefore the Peltier coefficient is defined as the ratio of the rate of heating or cooling at each junction to the current, as it is expressed by equation 1.2. The interdependency expressed by Thomson shows that there is a clear relationship between Peltier and Seebeck coefficients, as shown by equation 1.3. This is followed by Thomson Coefficient, τ, which is defined as the rate of heating per unit length that results from the passage of unit current along a conductor in which there is a unit temperature gradient, equation 1.4. For these coefficients, a positive value is indicative of the flow of current from the hot junction to the cold [9].

$$\alpha_{AB} = \frac{\Delta V}{\Delta T} \tag{1.1}$$

$$\pi_{AB} = \frac{q}{l} \tag{1.2}$$

$$\pi_{AB} = \alpha_{AB} T \tag{1.3}$$

$$\tau_A - \tau_B = T \frac{d\alpha_{AB}}{dT} \tag{1.4}$$

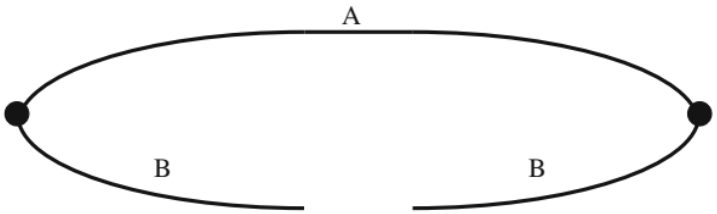

Figure 1.2: Simple thermocouple

1.3 Thermoelectric Devices

Irrespective of the temperature range where a material is used for thermoelectric application, there is a common phenomenon that is observed in thermoelectric materials. The ideal thermoelectric material creates a temperature gradient when it is exposed to heat from one side, while the other side keeps the same temperature as before heating. This implies that the material has low thermal conductivity. This temperature gradient results in the diffusion of charge carriers, and hence the potential difference between the two sides. This is the so-called Seebeck effect. The ratio of the resulted potential difference to the temperature gradient is called the Seebeck Coefficient. Therefore a large value of Seebeck coefficient is indicative of large potential difference as a response to a relatively small temperature gradient. A typical device structure and working mechanism are shown in figure 1.3.

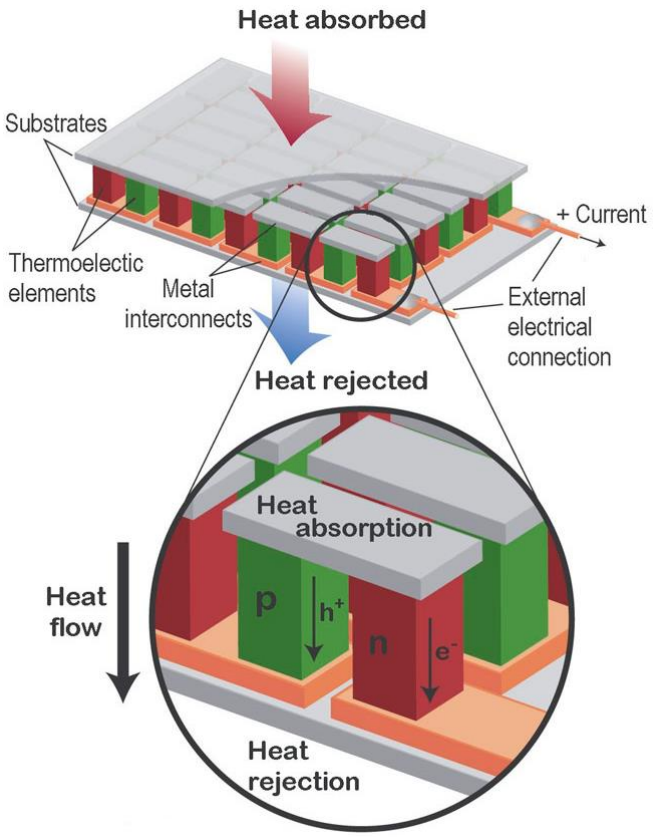

Figure 1.3: Working mechanism of thermoelectric material [10].

1.4 Thermoelectric Properties and Parameters

Like any other energy conversion process, for instance, hydropower or diesel engine, thermoelectric materials have theoretical efficiency. The efficiency directly shows the portion of energy (out of the total heat energy absorbed by the thermoelectric material) that is converted to electrical energy. This is described by a governing equation 1.5 [7]:

$$\eta = \left(\frac{T_H - T_C}{T_H}\right) \frac{\left(\sqrt{1+ZT}-1\right.}{\left(\sqrt{1+ZT}-(T_C/T_H)\right)} \qquad 1.5$$

where Z is the thermoelectric material property; T is the absolute temperature; ZT refers to the figure of merit of the material; T_C and T_H are the cold and hot side temperatures, respectively [11, 12].

The thermoelectric figure of merit, ZT, is given by equation 1.6 [13], where σ is the electrical conductivity, α is the Seebeck coefficient, and κ is the thermal conductivity. Heat transfer can take place due to either lattice vibration or a moving electron. This implies that a moving electron in a lattice has both electrical conductivity and thermal conductivity. Therefore the thermal conductivity of the system consists of two terms. One is the electronic contribution, k_e, to the thermal conductivity. The other is lattice contribution to the thermal conductivity, k_l. These are expressed by equation 1.7.

$$ZT = \frac{\alpha^2 \sigma T}{k} = \frac{\alpha^2 T}{\rho k} \quad 1.6$$

$$k = k_e + k_l \quad 1.7$$

Electrical conductivity can be determined from the measured electrical resistivity. According to Wiedemann–Franz relationship the electronic contribution to the thermal conductivity will be determined from the measured electrical conductivity [equation 1.8b]. The lattice thermal conductivity can be determined by subtracting the electronic component of the thermal conductivity.

$$k_T = k_e + k_l \quad 1.8a$$

$$k_e = \sigma L T = ne\mu L T \quad 1.8b$$

$$k_l = k_T - ne\mu L T \quad 1.8c$$

In fact, there is some deviation from this relationship [14]. On the other hand, each material has its own Lorentz number. This can be determined by simultaneously solving equations 1.9a-c [15-18]. Since acoustic phonon scattering is the dominant feature in thermoelectric materials, the scattering parameter for acoustic phonon scattering, characteristic of the scattering by the individual atoms, is taken as r = -1/2. For a specific value of S, if r is substituted in the equation 1.9c, the value of n for the equation 1.9b and hence fermi integral value in terms of η will be expressed, after solving the integral. This will give the value of $F_n(\eta)$ in terms of η. Substituting this expression back in the equation 1.9c gives an expression containing only η as a variable, and can be solved for its value. Hence the Fermi integral will have a specific value corresponding to the specific value of S (or as a function of the corresponding value of η). According to [16], the Lorentz number, L, can also be approximated numerically as shown by equation 1.10.

$$L = \left(\frac{k_B}{e}\right)^2 \left(\frac{(r+\frac{7}{2})F_{r+\frac{5}{2}}(\eta)}{(r+\frac{3}{2})F_{r+\frac{1}{2}}(\eta)} - \left[\frac{(r+\frac{5}{2})F_{r+\frac{3}{2}}(\eta)}{(r+\frac{3}{2})F_{r+\frac{1}{2}}(\eta)}\right]^2 \right) \qquad 1.9a$$

$$F_n(\eta) = \int_0^\infty \frac{x^n}{1+e^{x-\eta}}\,dx \qquad 1.9b$$

$$S = \pm \frac{k_B}{e}\left\{ \frac{(r+\frac{5}{2})F_{r+\frac{3}{2}}(\eta)}{(r+\frac{3}{2})F_{r+\frac{1}{2}}(\eta)} - \eta \right\} \qquad 1.9c$$

Where the reduced chemical potential, $= {E_f}/{k_B T}$, and E_f is the Fermi level energy.

$$L = 1.5 + \exp\left[-\frac{|S|}{116}\right] \qquad 1.10$$

For each phase, the type of charge carrier, Fermi energy and Bandgap can be determined. By analyzing the contacts at phase boundaries it will be possible to estimate the necessity of appropriate inclusion. A good thermoelectric material needs to have a high Seebeck coefficient

with high electrical conductivity while decreasing the thermal conductivity. The Seebeck coefficient directly refers to the amount of potential difference created for a unit change in temperature, i.e, it is the ratio of change of potential difference to that of temperature, as shown in equation 1.1. When heat energy is absorbed by a thermoelectric material, electrons will be excited and start to be mobilized to conduct electricity and heat. The larger the energy gap of the material, the higher will be the energy absorbed by the electron the more, hence the more will be the mobility of the electron. This results in large potential difference created for wider band gap materials. The relationship is shown in equation 1.11 [19]. The Seebeck coefficient varies with temperature. The T_{max} represents the absolute temperature at which the maximum value of the Seebeck coefficient occurs.

$$\alpha_{max} \approx \frac{E_g}{2eT_{max}} \tag{1.11}$$

$$\sigma = ne\mu \tag{1.12}$$

where n is the charge carrier concentration, and μ is the mobility of the charge carriers.

On the other hand, the electrical conductivity of thermoelectric materials decreases with increasing band gap of the material, shown by equation 6, since the only fewer number of electrons will be able to cross the energy barrier. This implies that it is difficult to achieve high values of both the Seebeck coefficient and electrical conductivity since there is a tradeoff between them [19]. Therefore it is important to consider another thermoelectric property called the power factor, S. It is the product of the square of the Seebeck coefficient with electrical conductivity, as shown in equation 13. Even though the value of S varies with temperature, the maximum value of S is an indicator of the high value of the figure of merit. Roughly, less carrier concentration leads to a high value of α, while σ increases with increase in concentration, this is shown in figure 1.4 [19].

This is usually true for any material. Insulators with very low charge carrier have high Seebeck coefficient, while conductors with high carrier concentration have very low value for Seebeck coefficient. Therefore the power factor will be high for semiconductors, which have a moderate value of carrier concentration, and hence Seebeck coefficient and electrical conductivity.

$$S = \alpha^2\sigma \qquad 1.13$$

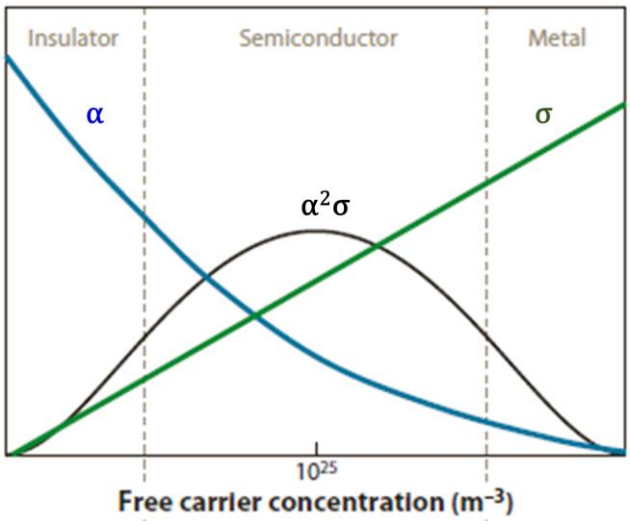

Figure 1.4: The variation of S, σ and α with carrier concentration [20].

There are various approaches [21-33] to decrease the thermal conductivity of thermoelectric materials. Both the electronic contribution and the lattice thermal conductivity can be manipulated to obtain a relatively high thermoelectric figure of merit. The propagation of phonon is the main reason for thermal conductivity by the lattice vibration. On the other hand, electrons that travel in the lattice while having low energy will contribute more to the thermal conductivity than to the electrical conductivity, and their energy will be transferred to the lattice in the form of heat energy. The presence of an energy barrier in the lattice helps to filter out such kind of electrons [34, 35]. T herefore, to introduce a defect site in the lattice is the main method to reduce both types of thermal conductivity. Alloying effects [25], grain refinement [21, 29, 31], nano-composites [21,

22, 31], intrinsic bond anharmonicity [28], and inclusions [23-27, 30, 32, 33] are some of the techniques used as state-of-the-art defect engineering strategies [13]. These techniques can be incorporated into different systems to improve the thermoelectric property of various materials. Both SnTe and Bi_2Te_3 are well known thermoelectric materials. But for practical application, the thermoelectric figure of merit should be at least 3. Until know the maximum value investigated is ~2.4 at 300 K for p-type Bi_2Te_3-Sb_2Te_3 superlattice thin film devices [36]. Therefore some of the above methods are expected to improve the thermoelectric property of the pseudo-binary Sn-Bi-Te system.

1.5 Thermoelectric Versus Pyroelectric Materials

Unlike the thermoelectric materials that needs a temperature gradient to generate electricity, the pyroelectric materials need time dependent varying temperature [37]. On heating/cooling in some materials (like gallium nitride (GaN) based materials, caesium nitrate ($CsNO_3$), Lithium tantalate ($LiTaO_3$, $LiNbO_3$)) voltage develops, this phenomenon is called pyroelectricity [38, 39]. On heating/cooling charge develops on the opposite faces of crystals lacking center of inversion. Heating leads to shift in atomic positions so as to lead to a voltage. As temperature change (stimulus) does not have a directionality, the response (polarization) must correspond to the symmetry of the crystal [40]. In all crystals with center of symmetry pyroelectricity is absent, i.e. if these type of crystals heated no charge/potential will develop. SnTe has space group of Fm-3m whereas the space group of both Bi and Bi_2Te_3 is R-3m. The symbol -3 represents the existence of a center of inversion (after a 3-fold rotation). The presence of center of inversion results in the absence of pyroelectric effect, during the study of the thermoelectric properties [40]. In addition these point groups are not part of the well-known ten point groups (1, 2, m, mm2, 3, 3m, 4, 4mm, 6, 6mm) that show pyroelectricity.

1.6 The Sn-Bi-Te system

Tin telluride, SnTe, is a small bandgap semiconductor with a direct gap of 0.18 eV [41], whereas bismuth telluride, Bi_2Te_3, has an indirect band gap of 0.13 eV, as it is investigated by Hada et al [42]. The Sn-Bi-Te pseudo-binary system has been studied for thin film and other applications [43, 44]. Some of the microstructural studies are accomplished by C.N. CHIU et al [45]. These studies are indicative of the possibility of having a thermoelectric Sn-Bi-Te system. Phase separation of different compositions enables to control the thermoelectric property as a function of composition. Some of the microstructures obtained by C.N. CHIU et al [45] are shown in figure 1.5, and the isothermal phase diagram obtained at 500 is shown in figure 1.6. The pseudo-binary phase diagram of SnTe-Bi_2Te_3 helps to estimate the possible phases that can be formed while varying the corresponding composition. As it is shown in figure 1.7, SnTe is a compound with the highest melting point. This gives a clear insight into the homogenization temperature which is required for the Bi-Sn-Te system.

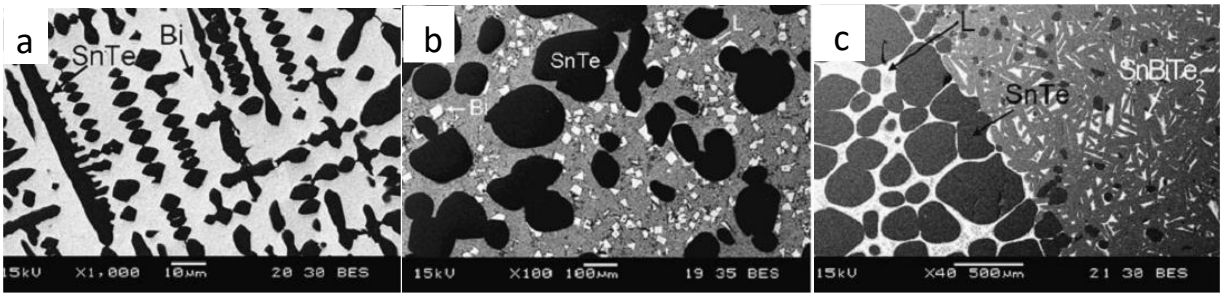

Figure 1.5: Back-scattered Electron Image micrographs of Sn-Bi-Te ternary alloys equilibrated at 500°C: (a) alloy of Sn-60.0 at.%Bi-20.0 at.%Te; (b) alloy of Sn-30.0 at.%Bi-20.0 at.%Te; and (l) alloy of Sn-30 at.%Bi-45 at.%Te. Adapted after [45].

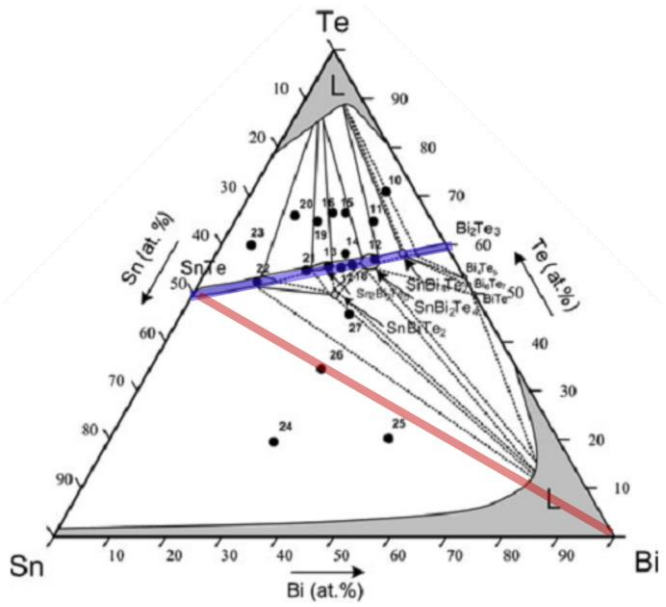

Figure 1.6: The ternary isothermal phase diagram, at 500 ℃, of the Sn-Bi-Te system. After [45].

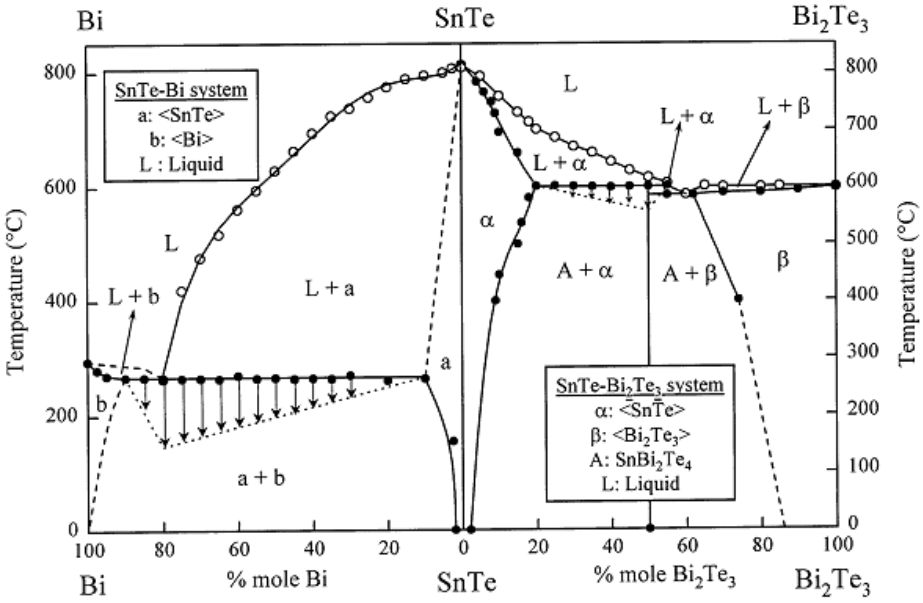

Figure 1.7: Phase diagram of the SnTe-Bi (left) SnTe-Bi_2Se_3 (right). Adapted after [46].

1.7 References

1. Rowe, D.M., *General Principles and Basic Considerations, In Thermoelectrics Handbook—Macro to Nano*. 2006, Boca Raton, FL, USA: CRC Taylor & Francis Group. 1–14.
2. Gray, P.E., *The Dynamic Behavior of Thermoelectric Devices*. 1960, New York, NY, USA: The Technology Press of The Massachusetts Institute of Technology and John Wiley & Sons, Inc.
3. Ioffe, A.F., *Semiconductor Thermoelements and Thermoelectric Cooling*. 1957, London, UK: Infosearch Limited.
4. Kittel, C., *Introduction to Solid State Physics* 6ed. 1974, Warsaw, Poland: PWN. 191 - 205.
5. Królicki, Z., *Thermodynamic Basis of Lowering the Temperature*. 2006, Wrocław, Poland: Wrocław University of Technology Publishing.
6. Wallace, G.S., G, *Conductive Electroactive Polymers Intelligent Materials Systems*. 2 ed. 2003, Boca Raton, FL, USA: CRC Press TFG. 125–175.
7. Kolasinski, E.K.a.P., *A Review on Electroactive Polymers for Waste Heat Recovery.* 2016. **9**(485).
8. Szargut, J., *Exergy Method: Technical and Ecological Applications*. 2005, Ashurst Lodge, UK: WIT Press.
9. Goldsmid, H.J., *Introduction to Thermoelectricity*. Springer Series in Materials Science. Vol. 121. 2009, Kingston Beach, Tasmania, Australia: Springer Nature.
10. Johnston, H. *Multiple valleys boost thermoelectric performance*. in *Physics World*. 2011.
11. Hostler, S.R.K., P.; Qu, V.; Cullen, C.; Abramson, A.R. *Thermal and electrical characterization of nanocomposites for thermoelectrics. In Proceedings of The Tenth Intersociety Conference on Thermal and Thermomechanical Phenomena in Electronics Systems*. 30 May–2 June 2006. ITHERM'06, San Diego, CA, USA.
12. Li, J.T., X.; Li, H.; Yan, Y.; Zhang, Q. , *Synthesis and thermoelectric properties of hydrochloric acid-doped polyaniline.* Synth. Met, 2010(160): p. 1153–1158.
13. Park, J.G. and Y.H. Lee, *High thermoelectric performance of Bi-Te alloy: Defect engineering strategy.* Current Applied Physics, 2016. **16**(9): p. 1202-1215.
14. Kolomoets, N.V., Sov. Phys. Solid State 1966. **8**(799).

15. Hu, L.-P., T.-J. Zhu, Y.-G. Wang, H.-H. Xie, Z.-J. Xu, and X.-B. Zhao, *Shifting up the optimum figure of merit of p-type bismuth telluride-based thermoelectric materials for power generation by suppressing intrinsic conduction.* Npg Asia Materials, 2014. **6**: p. e88.
16. Hyun-Sik Kim, Z.M.G., Yinglu Tang, Heng Wang and G. Jeffrey Snyder *Characterization of Lorenz number with Seebeck coefficient measurement.* APL Mat. 3, 041506 (2015).
17. Rhyee, J.-S. and J.H. Kim, *Chemical Potential Tuning and Enhancement of Thermoelectric Properties in Indium Selenides.* Materials, 2015. **8**(3): p. 1283-1324.
18. Xiao, Y., J. Yang, Q. Jiang, L. Fu, Y. Luo, D. Zhang, and Z. Zhou, *Synergistic tuning of carrier and phonon scattering for high performance of n-type Bi2Te2.5Se0.5 thermoelectric material.* Journal of Materials Chemistry A, 2015. **3**(44): p. 22332-22338.
19. Gibbs, Z.M., et al., *Band gap estimation from temperature dependent Seebeck measurement—Deviations from the 2e|S|maxTmax relation.* Applied Physics Letters, 2016. **108** (20): p. 209901.
20. Shakouri, A. *Recent Developments in Semiconductor Thermoelectric Physics and Materials. Annual Review of Materials Research*. 2011. Annu. Rev. Mater. Res.
21. Biswas, K., J. He, I.D. Blum, C.-I. Wu, T.P. Hogan, D.N. Seidman, V.P. Dravid, and M.G. Kanatzidis, *High-performance bulk thermoelectrics with all-scale hierarchical architectures.* Nature, 2012. **489**: p. 414.
22. Biswas, K., J. He, Q. Zhang, G. Wang, C. Uher, V.P. Dravid, and M.G. Kanatzidis, *Strained endotaxial nanostructures with high thermoelectric figure of merit.* Nature Chemistry, 2011. **3**: p. 160.
23. H.J. Kim, M.K.H., C.H. Yo, W.Y. Lee, S.J. Kim, *Effects of Bi2Se3 nanoparticle inclusions on the microstructure and thermoelectric properties of Bi2Te3-based nanocomposites.* J. Electron. Mater (2012) 41: 3411.
24. Kyung Tae, K., S. Injoon, and H. Gook Hyun, *Synthesis and Thermoelectric Properties of Carbon Nanotube-Dispersed Bi_2Te_3 Matrix Composite Powders by Chemical Routes.* Journal of Korean Powder Metallurgy Institute, 2013. **20**(5): p. 345-349.
25. Lee, E., J.I. Kim, S.-M. Choi, Y.S. Lim, W.-S. Seo, J.-Y. Kim, and K.H. Lee, *Thermoelectric Transport Properties of Cu Nanoprecipitates Embedded.* Journal of Nanomaterials, 2015. **2015**: p. 5.

26. Li, F., X. Huang, Z. Sun, J. Ding, J. Jiang, W. Jiang, and L. Chen, *Enhanced thermoelectric properties of n-type Bi2Te3-based nanocomposite fabricated by spark plasma sintering.* Journal of Alloys and Compounds, 2011. **509**(14): p. 4769-4773.
27. Liang, B., Z. Song, M. Wang, L. Wang, and W. Jiang, *Fabrication and Thermoelectric Properties of Graphene/ Composite Materials.* Journal of Nanomaterials, 2013. **2013**: p. 5.
28. Morelli, D.T., V. Jovovic, and J.P. Heremans, *Intrinsically Minimal Thermal Conductivity in Cubic $\mathrm{I}\mathrm{\text{\ensuremath{-}}}\mathrm{V}\mathrm{\text{\ensuremath{-}}}{\mathrm{VI}}_{2}$ Semiconductors.* Physical Review Letters, 2008. **101**(3): p. 035901.
29. Poudel, B., Q. Hao, Y. Ma, Y. Lan, A. Minnich, B. Yu, X. Yan, D. Wang, A. Muto, D. Vashaee, X. Chen, J. Liu, M.S. Dresselhaus, G. Chen, and Z. Ren, *High-Thermoelectric Performance of Nanostructured Bismuth Antimony Telluride Bulk Alloys.* Science, 2008. **320**(5876): p. 634-638.
30. Shaowei, S., W. Jueling, X. Bo, L. Xiaobo, J. Hongchuan, J. Yingrong, Z. Qinyong, and R. Zhifeng, *Thermoelectric properties of n-type Bi 2 Te 2.7 Se 0.3 with addition of nano-ZnO:Al particles.* Materials Research Express, 2014. **1**(3): p. 035901.
31. Zhao, L.-D., S. Hao, S.-H. Lo, C.-I. Wu, X. Zhou, Y. Lee, H. Li, K. Biswas, T.P. Hogan, C. Uher, C. Wolverton, V.P. Dravid, and M.G. Kanatzidis, *High Thermoelectric Performance via Hierarchical Compositionally Alloyed Nanostructures.* Journal of the American Chemical Society, 2013. **135**(19): p. 7364-7370.
32. Zhao, L.-D., B.-P. Zhang, J.-F. Li, M. Zhou, W.-S. Liu, and J. Liu, *Thermoelectric and mechanical properties of nano-SiC-dispersed Bi2Te3 fabricated by mechanical alloying and spark plasma sintering.* Journal of Alloys and Compounds, 2008. **455**(1): p. 259-264.
33. Zhang, Q., X. Ai, L. Wang, Y. Chang, W. Luo, W. Jiang, and L. Chen, *Improved Thermoelectric Performance of Silver Nanoparticles-Dispersed Bi2Te3 Composites Deriving from Hierarchical Two-Phased Heterostructure.* Advanced Functional Materials, 2015. **25**(6): p. 966-976.
34. Faleev, S.V. and F. Léonard, *Theory of enhancement of thermoelectric properties of materials with nanoinclusions.* Physical Review B, 2008. **77**(21): p. 214304.
35. I.H. Kim, S.M.C., W.S. Seob, D.I. Cheong, H. Kang, *Synthesis and thermoelectric properties of Cu-dispersed Bi2Te2.7Se0.3.* J. Ceram. Process. Res, 2012. **13**: p. 170-173.

36. Hansen, A.-L., T. Dankwort, M. Winkler, J. Ditto, D.C. Johnson, J.D. Koenig, K. Bartholomé, L. Kienle, and W. Bensch, *Synthesis and Thermal Instability of High-Quality Bi2Te3/Sb2Te3 Superlattice Thin Film Thermoelectrics.* Chemistry of Materials, 2014. **26**(22): p. 6518-6522.
37. Gael, S., G. Daniel, and A. Amen, *On thermoelectric and pyroelectric energy harvesting.* Smart Materials and Structures, 2009. **18**(12): p. 125006.
38. Nye, J.F., *Physical Properties of Crystals: Their Representation by Tensors and Matrices*. 1985, Oxford: Clarendon Press.
39. Newnham, R.E., *Properties of Materials: Anisotropy, Symmetry, Structure*. 2005, Oxford: Oxford University Press.
40. Fjellv˚ag, H., *Symmetry-operations, point groups, space groups and crystal structure*, 1994. p. 113 ,160 and 233.
41. Austin, I.G. *The Optical Properties of Bismuth Telluride. Proceedings of the Physical Society*. 1958.
42. Hada, M., et al, *Bandgap modulation in photoexcited topological insulator Bi2Te3 via atomic displacements.* The Journal of Chemical Physics, 2016. **145(2)**: p. 024504.
43. Banik, A. and K. Biswas, *Lead-free thermoelectrics: promising thermoelectric performance in p-type SnTe1−xSex system.* Journal of Materials Chemistry A, 2014. **2**(25): p. 9620-9625.
44. Banik, A. and K. Biswas, *Synthetic Nanosheets of Natural van der Waals Heterostructures.* Angewandte Chemie International Edition, 2017. **56**(46): p. 14561-14566.
45. Chiu, C.-n., C.-m. Hsu, S.-w. Chen, and H.-j. Wu, *Phase Equilibria of the Sn-Bi-Te Ternary System.* Journal of Electronic Materials, 2012. **41**(1): p. 22-31.
46. Adouby, K., A. Abba Touré, G. Kra, J. Olivier-Fourcade, J.-C. Jumas, and C. Perez Vicente, *Phase diagram and local environment of Sn and Te: SnTeBi and SnTeBi2Te3 systems.* Comptes Rendus de l'Académie des Sciences - Series IIC - Chemistry, 2000. **3**(1): p. 51-58.

CHAPTER 2

STATEMENT OF THE PROBLEM, SCOPE AND EXPERIMENTAL METHODS

2.1 Introduction

This chapter contains detail of the statement of the problem; the scope, experimental procedures; an overview of the methods, instrument, and techniques used for this work. The instruments include X-Ray diffractometer, Scanning Electron Microscopy (SEM), Electron Probe Micro Analyzer (EPMA), metallurgical microscope coupled with Vicker's hardness tester, Seebeck machine. In addition, the sample preparation techniques used for this work are also described in this chapter. The sample preparation method mainly includes non-equilibrium solidification; homogenization of some of the solidified alloys; aging of the homogenized samples, surface preparation, etc.…

This work has been conducted using Bi, Sn, and Te as reagents. All are more than 99.9 at% pure, elemental chunk and granules. The pseudo-binary phase diagram, shown in figure 1.6 was considered to select the compositions for this study. Accordingly, some compositions are taken from the Bi-SnTe side of the phase diagram. While others are taken from the SnTe-Bi_2Te_3 side. These samples are aimed to conduct two different experiments. The former focuses on the solubility of bi in SnTe phase and the consequence of this solubility on the microstructure, thermoelectric and mechanical property of the material while the latter focus on the solubility of Bi_2Te_3 in SnTe and the associated change in the microstructure and thermoelectric property. The detail of these experiments has been discussed in the next two chapters.

2.2 Statement of the Problem

Despite the fact that SnTe and Bi_2Te_3 are well known thermoelectric materials, the pseudo-binary Sn-Bi-Te system is relatively less investigated alloy system, especially for bulk microstructure and thermoelectric properties. This is found to be an open room for research. This research project is aimed to investigate the thermoelectric properties of some selected compositions from Sn-Bi-Te system. The variation of the composition, together with processing method, is expected to create microstructural variation. Since each phase will have different thermoelectric property, the property of the system will vary with the overall morphology. The nominal compositions studied in this part of the research are shown in table 2.1.

The Bi – SnTe region is aimed to find the right solubility of Bi in SnTe phase, which has a different value according to different research reports [1, 2]. Therefore firstly, this research focus on determining the value of the maximum solubility of Bi in SnTe phase, and the resulting microstructure, mechanical and thermoelectric property. The lack of information about the thermal stability of these materials is the other problem that has been addressed in this work. Secondly, in spite of the presence of some research works [3-5] regarding the thermoelectric property of some compositions in the SnTe-Bi_2Te_3 region, to the best of the author, the associated microstructure and thermodynamic phases are not well reported. This research will try to fill this gap by finding alternative phases in SnTe-Bi_2Te_3 region as potentially possible candidate microstructures for thermoelectric application. In general this research focuses on how did the microstructure, mechanical and thermoelectric properties of SnTe looks like in the presence of Bi secondary phase and Bi_2Te_3 addition?

#	Nominal Compositions (at %)			Remark
	Bi	Sn	Te	
1	1	49.5	49.5	Group 1 Bi solubility in SnTe
2	2.5	48.75	48.75	
3	7	46.5	46.5	
4	10	45	45	
5	13	43.5	43.5	
6	2.410	46.988	50.602	Group 2 Studying solubility of Bi_2Te_3 in SnTe.
7	8.696	39.130	52.174	
8	13.861	32.673	53.465	

Table 2.1: Nominal composition of the samples selected for this experiment.

2.3 Sample Preparation Techniques

2.3.1 Ingot Formation

The stoichiometric amount of each element is weighted and the mixture is sealed in a quartz tube under very low pressure, about 10-5 atm. Once evacuating the tube well, sealing the ends of the quartz tube was performed after softening by applying hot flame of the mixture of burning acetylene and oxygen. Naberturm box furnace was used to melt the samples at 900 ℃. The sealed tube was kept in an upright position in a furnace during the melting process, and it has been shacked repeatedly to ensure homogeneous distribution of the elements in the liquid state at 900 ℃. The samples get heated together with the furnace, and the melted liquid was kept at 900 ℃ for 2 Hrs. This is true for all of the samples, irrespective of their stoichiometry. The melting point of each element, as well as their possible compounds, are considered to decide the solution-treating temperature. SnTe melts around 808 ℃, which is the highest melting point among the possible substances in this work. On the other hand, tellurium has a high vapor pressure. Therefore, the

solution-treating temperature was chosen by considering the tradeoff between the loss of tellurium and better homogenization with increasing temperature. Based on the targeted aim of the samples different cooling processes are performed, this has been described in detail in chapter three and four. Generally, two cooling processes are included in this work. These are furnace cooling and rapid ice water quenching. A rough description of the effect of cooling rates is described as follows.

2.3.1.1 High Undercooling

High under-cooling refers to fast quenching of the melt from high enough temperature to room temperature or below room temperature. This gives very small time for diffusion process to take place, rather every atom will be part of a small particle. This results in the formation of many nucleation sites with very low growth rate [6]. Consequently, the finer particles will be present in an ingot of an alloy prepared by this method. Such kind of fine particle size may be good enough for thermoelectric property measurements without grinding (or milling) further to get finer particles.

2.3.1.2 Low Undercooling

Low under-cooling directly refers to a small change in the temperature while cooling the sample from the solution-treating temperature. In other words, it refers to a slow cooling process. This includes faster diffusion and hence fewer nucleation sits. As a result, the grain growth rate will be fast. Larger grains than that of a high undercooling process will result. The finer grains of high undercooling are more preferable for phonon scattering process since the smaller grains provide more grain boundary which is phonon scattering site. In fact, some researchers use even the larger grains of low undercooling, i.e. the ingot, without grinding or milling, for thermal conductivity measurement, for instance, Banik et al [7].

2.3.2 Surface Preparation

Both Vickers hardness testing and microscopy need surface preparation of the sample. The horizontal cross-sections were taken for this purpose. Once the ingot has been cut each piece had been mounted by mounting resin, for comfortable handling. The target surface is polished by different grid polishing papers (sandpapers). 8 to 2-micron meter diamond past was used for polishing, as a second step. Thirdly silica suspension was used for 10 for polishing fine scratches. After polishing the silica suspension was cleaned from the surface of the sample by distilled water and then dried by hot blowing air, using a hair drier. Aluminum foil had been used to avoid charging of the sample by the applied electron beam during characterization by electron probe micro-analyzer. To prevent contamination of the samples by dust, the samples had been kept in a roughly evacuated desiccator.

2.4 Characterization Techniques

2.4.1 X-Ray Diffractometer

Being the result of interference of light wave, called X-Ray, the XRD pattern of every crystalline system is unique. The scattering of X-Ray by each of the crystal plane will have strong constructive interference. This is the angle at which the corresponding peak will exist. As it is described by Bragg's law, the spacing of the planes has an inverse relationship with the sign value of the angle of reflection. This is explained by equation 2.1.

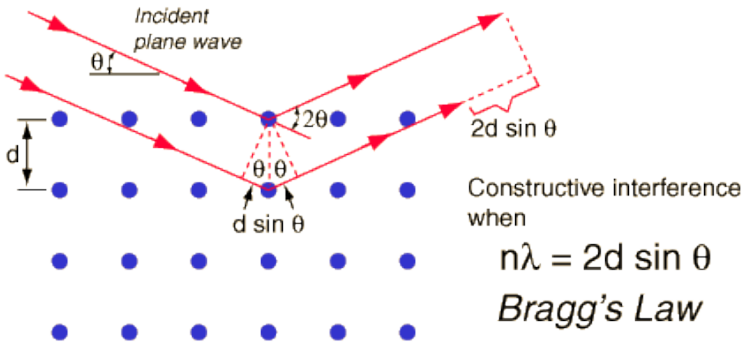

Figure 2.1: Bragg's law [8].

$$n\lambda = 2dsin\theta \tag{2.1}$$

λ is the wavelength of the radiation used, d_{hkl} the spacing of the crystal planes, and θ the angle of the diffraction peak. Since the wavelength of X-Ray is usually long enough compared to the spacing between the planes, the order of the reflection, n is taken as 1.

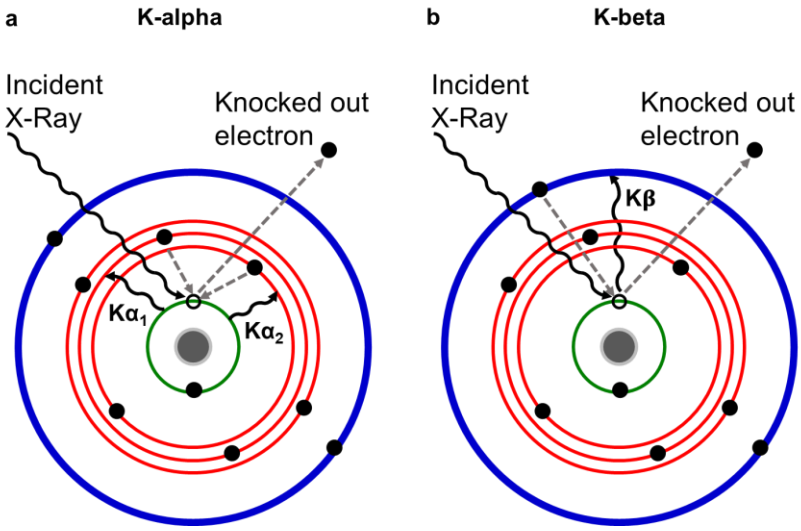

Figure 2.2: The principle of X-Ray scattering by electrons. (a) Generation of K-alpha and (b) Generation of K-beta.

Scattering of X-Ray takes place due to both an atom and electrons. The scattering of X-Ray by atoms in the crystal structure referred to us structure factor while that by electrons is scattering factor. Figure 2.2 shows the scattering of X-Ray and the consequent generation of k-alpha and k-

beta. When an atom is exposed to X-Ray its electron that has the lowest energy has a high probability to be knocked out by the incident X-Ray. Such an electron is found on the K shell. While the K shell electron is knocked out it will leave a hole behind, an electron that has higher energy will tend to minimize its energy. L or M shell electrons are the most probable electrons that can fill the hole. No matter where the electron comes to fill the hole the energy difference will be emitted as an X-Ray beam, which is characteristic of the atom. This energy will be changed even due to the energy difference between the sub-shells, especially if the sub-shells are that of L shell. If the sub-shell is the S-orbital of L shell the associated X-ray is called K-alpha 2, whereas that for P-orbital of L is K-alpha 1. If an M shell electron relaxes to fill the hole the associated X-Ray will be K-beta. In general the closer the subshell of the L shell to the K shell the less will be the associated energy difference and hence the longer will be the wavelength of the X-Ray.

In XRD system only K-alpha1 will play the most important role. This may be due to its highest probability of existence. K-alpha2 will be either stripped out or being modeled by software program during data analysis. This depends on the target information that will be obtained after the data analysis. In this work, K-alpha2 has been stripped out for phase identification and indexing, but during Rietveld refinement, it is advisable to consider it in the model. Almost all of the modern XRD instruments have monochromatic to filter out K-beta. Since K-beta has higher energy than K-alpha the monochromator can easily filter out K-beta.

2.4.1.1 Principle of Whole Pattern Profile Fitting

The intensity of the peaks is determined by the types and positions of the atoms in the crystal lattice according to the structure factor:

$$F(hkl) = \sum_{1}^{N} f_n \exp[2\pi i(hx_n + ky_n + lz_n) \quad 2.2$$

where hkl are the Miller indices of the reflecting planes, f_n the atomic structure factor, and x_n, y_n, and z_n, the coordinates of the n^{th} atom in the unit cell containing N atoms. In addition, the parameters of the equipment will affect the peak shape.

2.4.1.2 Crystallite Size and Microstrain Broadening

Anisotropic peak shapes can be identified by anisotropic peak broadening. If the dimensions of a crystallite are 2x*2y*200z, then (h00) and (0k0) peaks will be more broadened then (00l) peaks, i.e. the smaller the dimension the larger will be the corresponding peak broadening, as it can be seen from Scherrer equation. The dimensions of the crystallite which are perpendicular to the planes that produce the diffraction peak have some contribution to the peak broadening. The crystallite dimension may not be necessarily perpendicular, but the vector component of the dimension perpendicular to the plane will contribute to the peak broadening. This dimension is perpendicular to some plane that produces diffraction, but not parallel to the plane that produces the peak. Therefore the X-Ray diffracted from such kind of planes will not be as intense as the diffracting plane, nor will it exactly lie at the same angle, so that it will contribute to the peak broadening.

$$B_{crys} = \frac{k\lambda}{LCos(\theta)} \quad 2.3$$

$$B_r = \frac{k\lambda}{LCos(\theta)} + \eta Tan(\theta) \quad 2.4a$$

$$B_r Cos(\theta) = \frac{k\lambda}{L} + \eta Sin(\theta) \quad 2.4b$$

For crystallite size, L, X-Ray wavelength, λ, and a constant, k, the peak broadening due to crystallite size is expressed by the Scherer equation (equation 2.3). The other mechanism of peak broadening is the presence of strain, η. The resultant of the two peak broadenings, B_r, is described by Williamson-Hall equation, equation 2.4a or b. Equation 2.4b is used to find both strain and crystallite size of the system. Crystallite size and strain can be solved from the y-intercept and slop, respectively of equation 2.4b,

2.4.1.3 Rietveld Refinement

The XRD machine gives statistical data. The method to change this statistical data to a mathematical equation is called profile fitting. There are many methods for this process, called fitting or refinement. Rietveld refinement, Le Bail fit, Pawley fit, HKL-phase fit and Autoscaler fit are some of the fitting methods. Those methods and their importance for this research are discussed roughly as follows.

The principle of Rietveld analysis [9] is to iteratively compare the experimental pattern with a pattern simulated based on the presumed amounts, crystal parameters, and equipment parameters of a mixture of known phases. All these parameters may be adjusted between iterations to minimize the difference between experimental and simulated patterns by least squares fitting. Although the principle of the technique is straightforward [10]. A large number of parameters available means that a good ‘‘fit’’ may apparently be obtained for unrealistic values of the crystalline parameters and may be wrong values of the phase amounts [10, 11].

When the sample taken for powder XRD has more than one phase, the Rietveld analysis will solve the percentage of each phase, provided that all there is no amorphous phase. Therefore, all the phases present must be entered into the analysis and their crystal structures known. If amorphous

or unknown phases are present, the amounts of the crystalline phases estimated by the analysis will be higher than the true amounts present. This problem may be overcome by adding a known amount of a reference standard. The analysis may then be corrected by dividing the values by the ratio of the measured to the true amount of standard. The difference between the total of the corrected phase quantities and 100% gives the amount of amorphous (or unknown) phases [9]. Therefore to start Rietveld refinement there should be known phase and structure information, i.e. phases present in the sample and their respective space group and crystal structure also should be available. Peak positions are derived from unit cell and space group. Peak heights are calculated from the structure factors. Peak width and peak shape are constrained by mathematical functions changing slowly with 2Theta. The scale factor is calculated from the unit cell and from structure data; it can be used for quantitative analysis, such as weight percent of each phase [12].

2.4.1.4 Le Bail Refinement

Similar parameters as those that can be refined by Rietveld can also be refined by Le Bail refinement. The difference lies on the fact that Le Bail refinement doesn't need structural information to start the analysis, only phase information are enough. Peak positions are derived from unit cell and space group. Observed intensity is redistributed between overlapping peaks in an iterative way. Peak width and peak shape are constrained by mathematical functions changing slowly with 2Theta. There is no scale factor for quantitative calculations available [13]. Peak intensity is not refined. Therefore Le Bail fitting is one way of whole pattern profile analysis that can be performed with limited available initial information.

2.4.1.5 Pawley Refinement

This is another alternative to Le Bail fit that uses a structure-free approach, in which the intensities of the reflections are simply adjusted to fit the observed ones to obtain initial values for the profile

parameters [14]. Only phase information may be required. Each peak height is fitted individually. Peak width and peak shape are constrained by mathematical functions changing slowly with 2Theta. There is no scale factor for quantitative calculations available [12]. Le Bail and Pawley refinement can also serve as ways of checking how good the Rietveld refinement is. If the goodness of fit of Rietveld refinement is much larger than one, the goodness of fit of the corresponding structure-free refinement determined. If the crystallographic fit of Rietveld refinement is as good as the Pawley/Le Bail fit, then experimental features in the data typically peak shape or background are not being modeled properly, but the crystallographic model can no longer be improved [11].

In this work, X-ray diffraction data were collected using Cu-Kα radiation with XPERT-PRO X-ray diffractometer having an X'CELARATOR detector. The resulting data are analyzed by X'Pert HighScore Plus software. Even though the goodness of fit found Rietveld refinement was good enough, the Le Bail and/or Pawley fit is taken as a reference to check how good the model is, used for Rietveld refinement. The scanning was taken between 10 and 110 degree 2theta, with a step size of 0.033 degrees and a total time of 48 minutes.

2.4.2 Microscopy

ESEM and EPMA are used for characterizing the samples morphology, composition and for imaging. The instruments' models are ESEM Quanta 200, FEI makes; and JEOL make JXA-8530F Electron Prob Microanalyzer, respectively. Electron microscopy has mainly be used for phase determination, stoichiometry identification of the phases. The techniques used during this characterization include elemental mapping, line analysis, and point analysis. Both Energy Dispersive Spectroscopy, EDS, and Wavelength Dispersive Spectroscopy, WDS, were tested to choose the convenient one for the system of the sample used in this analysis. The detectors found

in EPMA includes secondary electrons detector, backscattered electrons detector, characteristic X-ray detector. The secondary electron mode of the SEM is used to see the morphology of the sample, mainly to check the effect of the silica suspension used for the final step of polishing the sample, since it can also have etching effect.

The secondary electron images are taken to analyze the composition of the sample, and hence to identify the phases present in the sample. The characteristic X-ray is useful to identify the elements presented in the different phases. While the secondary electron image was analyzed together with information from the X-ray detector, in that the WDS system was found to be good for determining the elements present in a required phase of the sample. In other words, the composition founded by EDS wad completely different from the original composition, and have more than 10 % difference with that obtained by WDS. This may be due to the limitations of EDS [15], which has relatively poor energy resolution. Elemental mapping, which uses the combination of WDS and EDS, was also taken for some samples to check the distribution of the elements in the microstructure.

2.4.3 Determining Volume Fraction by Systematic Manual Point Count

An electron microscopy image can be analyzed to get the volume fraction of phases contained in it. The technic recommended by ASTM is Determining Volume Fraction by Systematic Manual Point Count [16]. This method is more recommended than image binarization, using software programs. The method relays on the fact that the areal fraction of a phase is equal with the probability of getting a randomly taken point, out of the total area of the image, in the area covered by the phase. Therefore uniformly distributed square grid points were preferred for applying the procedure. Even though the ASTM procedure allows to visually estimate the areal fraction, image

binarization was used using ImageJ software to roughly estimate the area fraction, so as to choose the number of points needed to construct the square grid. Accordingly, 49 points were taken, in 7×7 square grid.

When square grid falls on a randomly selected area of the image, the number of target phase on which the point of the square grid falls will be counted as one point. If the target phase only touches the point of the square grid or when it is doughty it will be counted as half of a point. The ratio of overall points that falls on the target phase to that of the total number of points of the square represents the volume fraction of the target phase under consideration. The average value for, $\bar{P}_f$, the phase fraction, P_f, form each field, i, can be calculated from equation 2.4a. The 95% Confidence Interval, 95% CI, where this average value can be found is calculated from the standard deviation, s, as shown by equation 2.4c. Hence the volume fraction, V_f, an estimate is given by equation 2.4d.

$$\bar{P}_f = \frac{1}{n}\sum_{i=1}^{n} P_f(i) \qquad 2.4a$$

$$s = \left[\frac{1}{n-1}\sum_{i=1}^{n}\left[P_f(i) - \bar{P}_f\right]^2\right]^{1/2} \qquad 2.4b$$

$$95\%\ \mathrm{CI} = \mathrm{t} \times \frac{s}{\sqrt{n}} \qquad 2.4c$$

$$V_f = \bar{P}_f \pm 95\%\ \mathrm{CI} \qquad 2.4d$$

where t is 95 % confidence interval multiplier, taken from ASTM standard [16]. Its value depends on the number of fields, n. An estimate of the percentage relative accuracy, % RA, associated with the estimate, which is calculated from the above 95% CI is given by equation 2.5.

$$\%RA = \frac{95\%\ \mathrm{CI}}{\bar{P}_f} \times 100 \qquad 2.5$$

2.4.4 Vickers Hardness Tester

Vickers hardness was tested by a commercially available instrument, Future-Tech Corporation, which is equipped with a metallurgical optical microscope, and have a pyramidal diamond tip. The optical microscope was used to see the micro-indentation during the testing, accordingly, the diagonals of the two-dimensional image, while considering the magnification, were taken to calculate the Vickers hardness in an automatic computerized system, as shown in equation 2.6 A 25 g load was applied for 10 sec during this testing. For each sample, about ten spots have been taken to find the Vickers hardness value, and the average and standard deviation of the date are calculated. The spots have been taken by keeping one far enough from the other, so as to prevent strain hardening during the measurement.

$$HV = \frac{1.8544F}{d^2}(kgf/mm^2) \qquad 2.6$$

2.4.5 Seebeck Coefficient and Electrical Resistivity

Seebeck coefficient and electrical resistance are measured simultaneously using ULVAC-RIKOZEM-3 M10, in Helium environment. The samples prepared for this measurement are rectangular cylinder bars with dimensions ~2.4 mm × 2.1 mm ×12.3 mm. The electrical resistance was measured using a four probe method. The instrument is a computerized system, hence the software installed enables it to get electrical resistivity instead of electrical resistance. The four probe method gives more accuracy than that of a two probe method. The latter keeps the two probes in serious with the sample being measured, and measures both current and voltage by those

same probes. This adds the voltage drop on the contact resistance on that of the sample, i.e. the contact resistance will be added to the resistance of the sample. Unlike the two probe method, the four probe method measures the voltage in parallel by other pairs of probes, hence avoiding the contact resistance.

Electrical conductivity can be determined from the measured electrical resistivity, from those the lattice thermal conductivity will be determined by subtracting the electronic component of the thermal conductivity according to the Wiedemann–Franz relationship, shown by equations 1.8a to c. For each phase, the type of charge carrier, Fermi energy and Bandgap can be determined. By analyzing the contacts at phase boundaries it will be possible to estimate the necessity of appropriate inclusion.

2.5 Scope

This project covers the investigation of the different microstructure formed by the Sn-Bi-Te system, and determination of the corresponding thermoelectric properties. The microstructural study will include researching the solubility of Bi in SnTe phase, which has a different value according to different researchers [1, 2]. The thermoelectric property will be studied to examine the simultaneous effect of Bi dopant on the SnTe and that of the Bi secondary phase. Investigation of the change in the mechanical property of the Bi-SnTe system is the other aim of this research, which is aimed to determine the thermal stability of the material by aging. The research on the region of SnTe-Bi_2Te_3 focuses on determining different microstructures which may have potential application for thermoelectric devices. The study of microstructure variation focuses on the effect of both composition and processing method. The samples will be compared in terms of their thermoelectric properties.

2.6 General Objective

- ✓ Investigation of the thermoelectric properties of the pseudo-binary Sn-Bi-Te system is the general objective of this research.

2.7 Specific Objective

- ✓ Investigating different thermodynamic phases of the pseudo-binary Sn-Bi-Te system.
- ✓ Analyzing the thermoelectric properties as a function of composition and phase fraction.
- ✓ Determining the better combination of phases for effective thermoelectric applications.

2.8 References

1. Freik, D.M., S.I. Mudryi, I. Gorichok, V. Prokopiv, O. Matkivsky, I.O. Arsenjuk, O.S. Krynytsky, and V.M. Bojchyk, *Thermoelectric Properties of Bismuth-Doped Tin Telluride SnTe:Bi*. Vol. 61. 2016. 155-159.
2. Adouby, K., A. Abba Touré, G. Kra, J. Olivier-Fourcade, J.-C. Jumas, and C. Perez Vicente, *Phase diagram and local environment of Sn and Te: SnTeBi and SnTeBi2Te3 systems.* Comptes Rendus de l'Académie des Sciences - Series IIC - Chemistry, 2000. **3**(1): p. 51-58.
3. al, R.A.R.e., *Phase Relations and Thermoelectric Properties of the Alloy Systems SnTe - Bi2Te3 and PbTe - Sb2Te3.* J. Electrochem. Soc., 1967 **114**(5): p. 526-529.
4. Xisong, Z., N. Jun, W. Junbo, and N. Ce Wen. *Thermoelectric properties and microstructure of SnTe-Bi/sub 2/Te/sub 3/ alloys*. in *Proceedings ICT2001. 20 International Conference on Thermoelectrics (Cat. No.01TH8589)*. 2001.
5. Zhou, X.-S., Y. Deng, C.-W. Nan, and Y.-H. Lin, *Transport properties of SnTe–Bi2Te3 alloys.* Journal of Alloys and Compounds, 2003. **352**(1): p. 328-332.
6. William D. Callister, J., *Materials Science and Engineering: An Introduction*. 7th ed., United States of America: John Wiley & Sons, Inc.
7. Banik, A., U.S. Shenoy, S. Saha, U.V. Waghmare, and K. Biswas, *High Power Factor and Enhanced Thermoelectric Performance of SnTe-AgInTe2: Synergistic Effect of Resonance Level and Valence Band Convergence.* Journal of the American Chemical Society, 2016. **138**(39): p. 13068-13075.
8. Available from: http://hyperphysics.phy-astr.gsu.edu/hbase/quantum/bragg.html, visited on september 20, 2018.
9. Rietveld, H.M., *A profile refinement method for nuclear and magnetic structures.* Journal of Applied Crystallography, 1969. **2**(2): p. 65-71.
10. Scrivener, K.L., T. Füllmann, E. Gallucci, G. Walenta, and E. Bermejo, *Quantitative study of Portland cement hydration by X-ray diffraction/Rietveld analysis and independent methods.* Cement and Concrete Research, 2004. **34**(9): p. 1541-1547.
11. Toby, B.H., *R factors in Rietveld analysis: How good is good enough?* Powder Diffraction, 2012. **21**(1): p. 67-70.
12. YOUNG, R.A., *The Rietveld Method*. 1993, paperback (1995, 2000), Oxford Oxford University Press.

13. Le Bail, A., H. Duroy, and J.L. Fourquet, *Ab-initio structure determination of LiSbWO6 by X-ray powder diffraction.* Materials Research Bulletin, 1988. **23**(3): p. 447-452.
14. McCusker, L.B., R.B. Von Dreele, D.E. Cox, D. Louër, and P. Scardi, *Rietveld refinement guidelines.* Journal of Applied Crystallography, 2007. **32**(1): p. 36-50.
15. KAPLAN, D.B.A.W.D., *Microstructural Characterization of Materials*. 2nd ed. 2008, Technion, Israel Institute of Technology, Israel: John Wiley and Sons, Ltd. p 341-343.
16. Testing, A.S.f. and Materials, *ASTM E562-01: Standard Test Method for Determining Volume Fraction by Systematic Manual Point Count*. 2002: ASTM.

CHAPTER 3

MICROSTRUCTURAL, MECHANICAL AND THERMOELECTRIC PROPERTIES of SnTe SYSTEM WITH Bi SECONDARY PHASE

3.1 Introduction

The interdependence of some of the thermoelectric properties needs careful investigations to improve the performance of the devices. The improvements include the electrical conductivity of the material while decreasing its electronic thermal conductivity, which is strongly interdependent. Decreasing the lattice thermal conductivity is the other method that can help to decrease the total thermal conductivity of the material.

On the other hand improvement of the thermoelectric figure of merit usually needs to filter out low energy electrons and to prevent bipolar contribution to the electronic thermal conductivity [1]. This approach usually needs increasing the band gap of the material, which enables the filtration of high energy electrons. Though this method can decrease the electrical conductivity, it will improve the Seebeck coefficient. While compromising the tradeoff between Seebeck coefficient and electrical conductivity, the former plays a vital role than the latter due to its squared relation to the power factor, as shown by equation 1.13. Improvements on electronic properties usually achieved by using dopants, whereas properties related with phonon properties are achieved mostly by the metallurgical approach or all scale hierarchical architecture method [2, 3].

Different reported approaches can increase device performance. The simultaneous existence of an increase in the electronic band gap and convergence of light and heavy hole bands is one of the reported approaches [4, 5]. This directly enhances the carrier concentration near the valence band

maximum (tend to increase electrical conductivity), and increase the energy band gap (hence increase the Seebeck coefficient). In other words, band gap convergence activates the high effective mass valence bands and make them contribute for the carrier concentration. Silver [4] and Magnesium [5] are well-known dopants that increase the principal band gap of SnTe. The introduction of indium dopant can create resonant states near the Fermi level of the SnTe [4, 5]. Therefore co-doping of Ag and In, or Mg and In on SnTe can enable to utilize the synergistic effect of increasing band gap, valence band convergence and resonance states to increase the Seebeck coefficient and electrical conductivity. Mn [6], Cd [7], Ca [8] and Hg [9] also have a similar effect of increasing the principal electronic band gap of SnTe.

All scale hierarchical engineering [3] is the other approach used in some thermoelectric materials. This method is aimed to increase the scattering of phonon by deferent mechanisms, such as non-inclusions, grain boundary scattering, point defects, and dislocations. When the dopant concentration increases a little more than its solubility limit, it will form nano-precipitates [10]. These point defects and precipitates are efficient in scattering high-frequency phonon [3]. Dislocations, which usually can be introduced by deformation, scatters mid frequency phonon. Grain boundaries scatter low-frequency phonon. These all defects can be simultaneously introduced into the thermoelectric material and be able to minimize all range of frequency phonons. In addition to the low figure of merit, thermoelectric materials have several limitations. These include thermal and mechanical stability of the material, a problem of composition difference of the thermoelectric legs, low range of working temperature, and electrode contact resistance [11].

Bismuth-containing SnTe system has been studied by different researchers [10, 12, 13], from different perspectives including the solubility of Bi and its effect on SnTe phase, as non-

stoichiometric dopant, to study the simultaneous effect of Bi dopant and Bi precipitate, change in mechanical property of SnTe in the presence of Bi dopant and so on. There is a report on the phase diagram of the Bi-SnTe pseudobinary system that can give some insight for further study on this system [14]. Despite the presence of these researches, some conflicting information are also there in some of them, for instance, the solubility limit of Bi in SnTe phase has been reported with significantly different values by two of the reports [12, 14]. The response of the thermoelectric material, SnTe in the presence of Bismuth, for change in concentration, aging, and other related parameter are discussed in this research.

Bismuth is a semi-metal with low thermal conductivity. This property may help to reduce the thermal conductivity of Bi-doped SnTe. Lattice anharmonicity, which is expressed by the chemical bonding of the constituent elements, is one mechanism of reducing thermal conductivity [15]. Anharmonicity of the chemical bond drives the phonon-phonon umklapp and normal processes that intrinsically limit the high-temperature lattice thermal conductivity [16]. Octahedral coordination in the rock-salt semiconductors such as PbTe has a high degree of anharmonicity, which lowers their lattice thermal conductivity, k_{lat}, by about a factor of 4 compared to tetrahedrally bonded semiconductors with similar or better electronic properties such as GaAs, InAs, and InSb [17].

This chapter aims to investigate the change in microstructural and thermoelectric properties as a function of Bi concentration and the change in mechanical property as a function of composition and aging. Three different compositions, from the SnTe-Bi system, are chosen based on the solubility of Bi in SnTe system. According to Adouby et al. [14], the solubility limit of Bi into SnTe is ten at% Bi. The three samples are taken from Bi soluble region, the solubility limit, and from Bi saturated region; these are seven at%, ten at% and 13 at% Bi. After analyzing the two

samples, some more samples have been taken from less Bi concentration side. The target of the latter samples was to both approve the anomalous solubility compared to Adouby et al., and to consider the compositions for thermoelectric property measurements.

3.2 Experimental

3.2.1 Material Synthesis

The stoichiometric amount of 99.9 at% purified reagents was used to prepare each of the samples. Each of the samples was poured in the quartz tube, and the tube had been evacuated until the inside pressure reaches 10^{-5} atm. After maintaining this pressure, the tube was sealed by using a purge flame from burning acetylene with oxygen. The flame was used to make the quartz tube soft enough to be sealed. Figure 3.2 shows the setup used during the sealing process of the samples. Once after sealing the pressure difference between the inside and outside of the tube is used to check the absence of error during the process. Heating the tube by the purging flame softens it which will create bump to the inside of the tube, provided that there is no leakage of air to the inside of the tube. The procedure followed during sample preparation and characterization are summarized by the flow chart shown in figure 3.1.

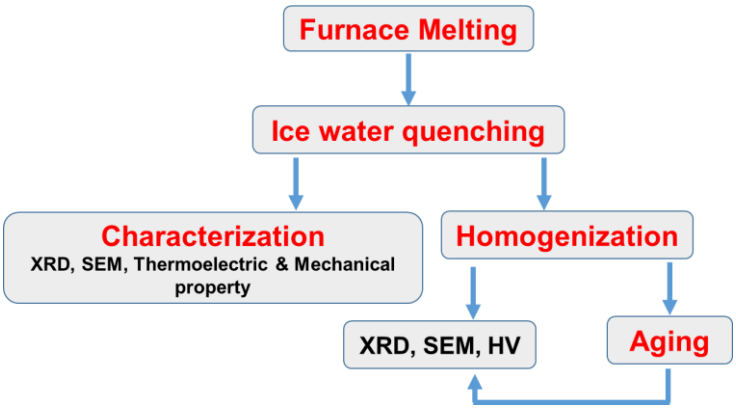

Figure 3.1: Flow chart of synthesis and characterization.

Sample name	Nominal Composition, at %		
	Bi	Sn	Te
SB1	1	49.5	49.5
SB25	2.5	48.75	48.75
SB7	7	46.5	46.5
SB10	10	45	45
SB13	13	43.5	43.5

Table 3.1: The nominal composition of the samples.

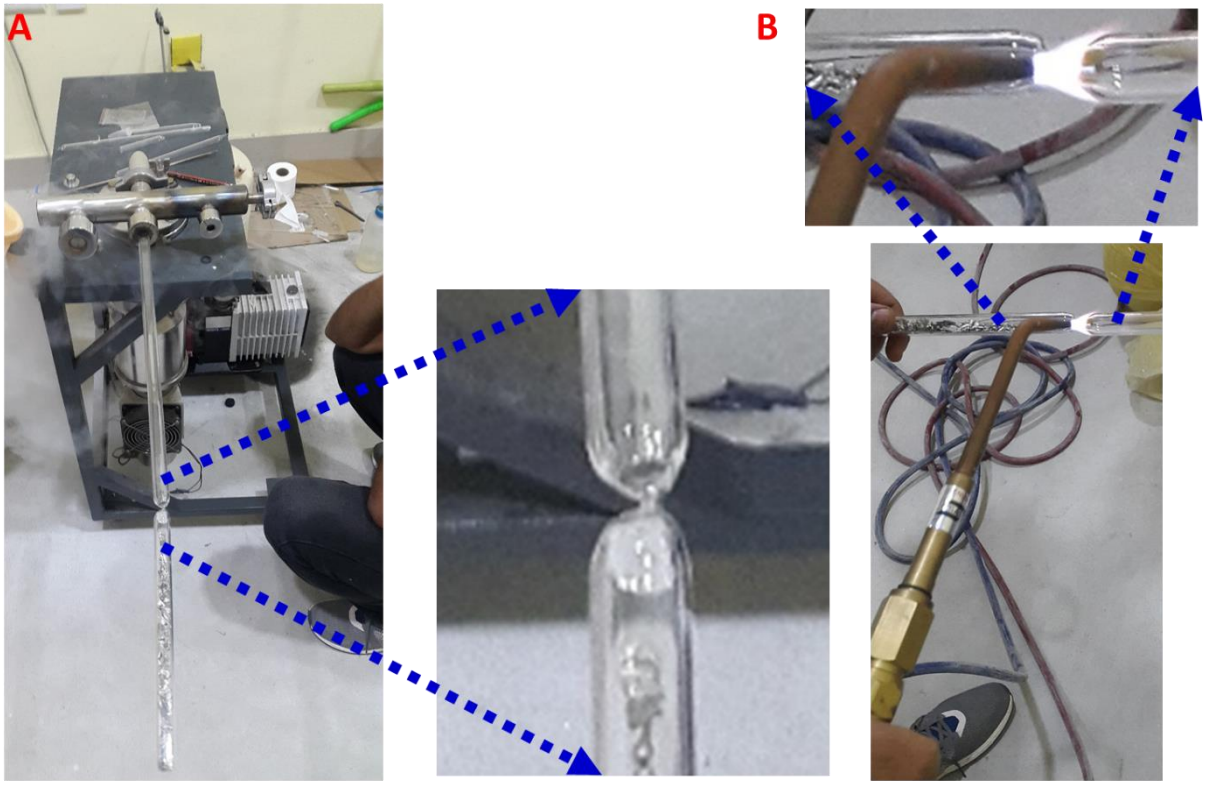

Figure 3.2: The setup used during the sealing process of the samples. (a) Evacuating the tube contains the sample. (b) Sealing by purging flame.

The samples were kept in an upright position inside a box furnace at room temperature. The box furnace was heated to 900 ℃ in 4 hrs and was kept at this temperature for 2 hrs while shaking the quartz tube frequently to provide a homogeneous distribution of the reagent elements in the samples. Finally, ice water quenching was used to cool down and form the ingot. Since the quartz tube has low heat capacity, which makes it release heat fast during cooling, it has been preferred not to break it while quenching. The sealed quartz tube helps to prevent contamination of the sample by the quenching medium.

The thermoelectric property was studied both for the as-quenched ingot and after hot-pressing the powder of the ingot into pellet. The hot-pressing was conducted using induction hot-pressing system at 673 K and 40 MPa for 6 minutes. The extent of compaction of the pellets were determined according to Archimedes principle. The relative density was taken as the ratio of the dry weight to the difference between the wet weight and the submerged weight. The percentage compaction was taken as the ratio of the relative density to the reported value of the density of Sn_3BiTe_4. About 86.0 and 85.5 % compaction were obtained for SB7 and SB10, respectively. The microstructure and X-Ray diffractions were studied both before and after hot-pressing.

3.2.2 Microscopic Characterizations

The horizontal cross-section of each ingot was taken for microscopy and mechanical property characterizations. Some other pieces of the ingot were powdered and characterized by XRD, using Cu-Kα radiation with XPERTPRO X-ray diffractometer having an X'CELARATOR detector. Irrespective of the Bi concentration, its solubility was very low, so that only SB7 and SB10 samples were taken for mechanical property determination. The ESEM and EPMA instruments' models are

ESEM Quanta 200, FEI makes; and JEOL makes JXA-8530F Electron Prob Microanalyzer, respectively.

For ESEM and EPMA analysis, the samples' surface were prepared by polishing using different grid polishing papers, up to 3000 grid paper. This step was followed by cloth polishing with the diamond suspension of 2 to 8 μm size. To clear fine scratches silica suspension was used for polishing in a vibratory polisher machine for 10 hrs. Cleaning of the polishing chemicals was accompanied by sonicator using distilled water for 20 minutes sonication and then drying the surface by hot blowing air, using hair dryer reserved for this purpose.

It is the cross-section of the ingots that have been characterized for this experiment. To check the existence of directionality of the phases during solidification EPMA image of SB7 has been taken both in the horizontal and vertical cross-section of the ingot. The images show that there is no special directional solidification; instead, both images show a similar nature in the distribution of the phases. On the other hand, the EPMA elemental analysis shows that there is no significant change in solubility of Bi in SnTe phase with the duration of aging. Since the images change in the size of the Bi secondary phase with the change in aging time, it is essential to check if there is a change in the overall volume fraction of Bi due to aging.

Determining Volume Fraction by Systematic Manual Point Count

Two methods obtain the fractions of the phases. One was using Rietveld refinement. The other was using the procedure recommended by ASTM E562-01 [18], which is Volume Fraction by Systematic Manual Point Count. The Rietveld refinement directly gives the weight percentage of the phases. It also gives the calculated density of the phases; while the ASTM E562-01 procedure gives the volume fraction by analyzing the electron microscopy images. Even though the ASTM

E562-01 procedure allows to estimate the areal fraction visually, image binarization was used using ImageJ software to roughly estimate the area fraction, to choose the number of points needed to construct the square grid. Accordingly, 49 points were taken, in 7×7 square grid. The distance between the points was approximately double of the size of the Bi phase. For better accuracy, five image with different magnifications, and two fields from each image were taken.

3.2.3 XRD and Rietveld Refinement

It is reported by Brian Toby [19], there is a lack of a generalized rule to identify how proper the fitting is good enough while comparing the observed XRD curve with that of the calculated by Rietveld refinement. The measure of goodness of fit, called Chi-square, should theoretically be 1. In practice, it can even be $\chi^2 \gg 1$. When it is not possible to improve, it will be advisable to compare it with Le Bail or Pawley fit, neither of them needs constraint of a structural model. If the crystallographic fit is as good as the Pawley/Le Bail fit, then experimental features in the data, typically peak shape or background, are not being appropriately modeled, but the crystallographic model can no longer be improved. In this work, it has been found that the Chi-square value is a bit larger than 1. Even though such deviation is usual [20], the Le Bail fit is also presented for a matter of comparison of the model. Many enough parameters, compared to other literature [21], have been considered during the Rietveld refinement. Relatively poor fitting is observed for some peaks with a strong effect of k-alpha2. The small difference between the Chi-square values of the Le Bail fit and Rietveld analysis implies that the crystallographic model can no longer be improved.

Since the density obtained from Rietveld refinement was calculated by considering the change in density due to a little number of dopants, i.e., Bi in SnTe phase and Sn and Te in Bi phase, it was preferable than the density of pure SnTe and Bi. Therefore changing the weight fraction obtained

from Rietveld refinement to volume fraction was preferable to compare the phase fractions obtained by the two methods.

3.2.4 Mechanical Property Testing

The samples for the Vickers hardness test also prepared by the same procedure, except for the total amount. Each of these ingots was large enough to cut them into pieces and age each sample for different aging time, after being homogenized at 267 ℃ for 12 hrs. After every heat treatment, a piece of each sample was taken for characterization by SEM and XRD. This characterization was in the same way as what has been done for the as-quenched ingot. Vickers hardness, HV, the test was performed using a commercially available instrument, Future-Tech Corporation, which is equipped with a metallurgical optical microscope, and have a pyramidal diamond tip. 25 g-force was applied for 10 Sec during the HV test.

The optical microscope was used to see the micro-indentation during the testing. Accordingly, the diagonals of the two-dimensional image, while considering the magnification, were taken to calculate the Vickers hardness in the automatic computerized system. It is those samples that had been used for microscopy, then used for HV test. Some more surface preparation was taken in order to identify the phases by the optical microscopy of the HV tester. The surface of the samples was etched by 10 % concentrated hydrochloric acid for 1 min. This etching slightly dissolves the Bi phase. About ten indents were taken to calculate the average and standard deviation of the HV. The indents are taken on the SnTe phase, by looking for a relatively wide are compared to the indenter size. This limited number indents were preferred to keep one indent far enough from the other, i.e., to avoid strain hardening during the HV test.

3.2.5 Thermoelectric Property Measurement

The same procedure also synthesized the samples for thermoelectric property measurement. All of them were as-quenched samples. The ingots had been cut to maintain a rectangular bar shape. The dimensions of these samples were ~2.4 mm × 2.1 mm × 12.3 mm. Seebeck coefficient and electrical resistance are measured simultaneously using ULVAC-RIKOZEM-3 M10, in Helium environment. The measured temperature dependent Seebeck coefficient were used for determining the Lorentz number according to equation 1.10. The electronic thermal conductivity was calculated for the Lorentz number and electrical conductivity, using equation 1.8b. The values of the Seebeck coefficient and electrical conductivity, which was calculated from the measured electrical resistivity, were also used to calculate the power factor as a function of temperature.

3.3 Results

3.3.1 Microstructure Analysis

The microstructural images and associated data obtained from electron microscopy were analyzed from different views. The WDS data was used to estimate the solubility of Bi in SnTe and to determine the composition of the phases in the system; the images directly shows the number of phases present in the system. Additionally, the fraction of the phases, calculated by the ASTM procedure, were used to confirm that of the Rietveld refinement. The phase determined by electron microscopy was used to confirm that of the XRD result.

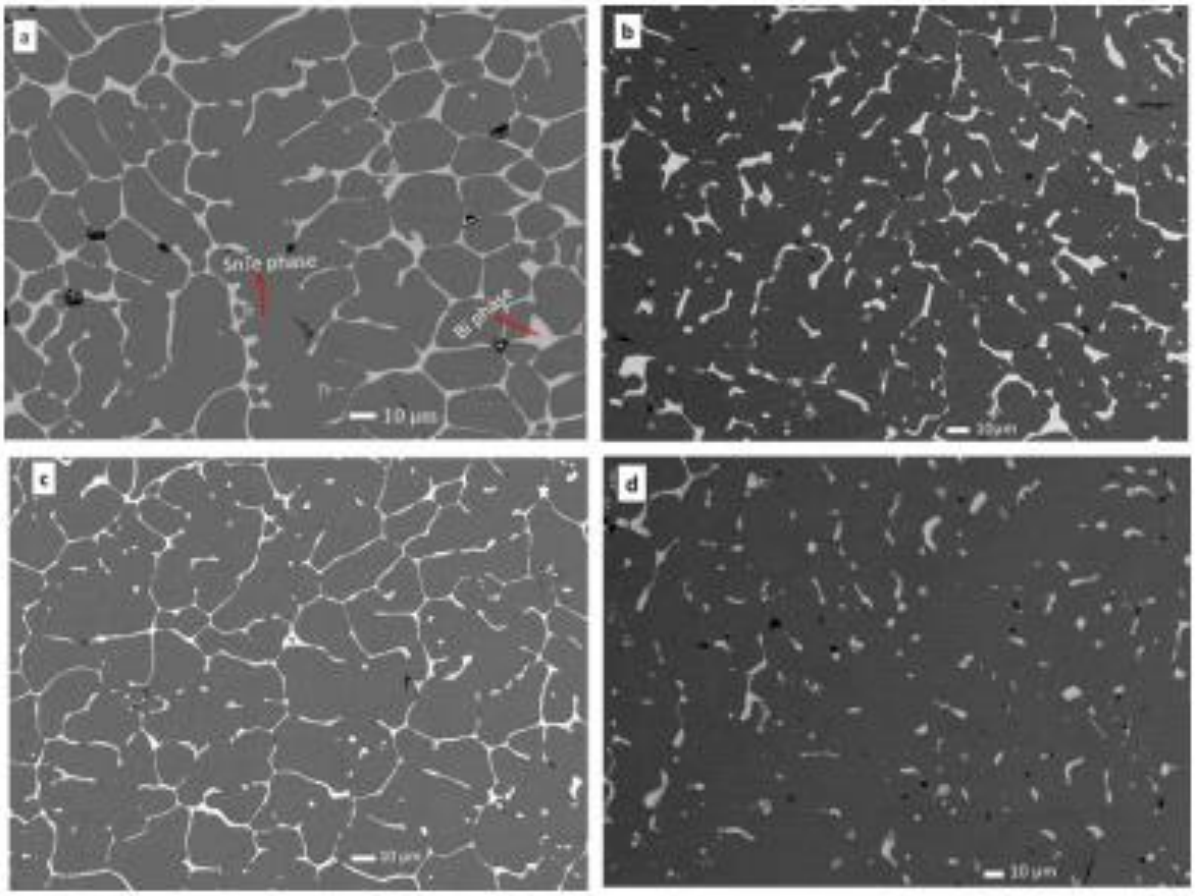

Figure 3.3: SEM image of (a) as quenched SnTe - 10 at % Bi (b) SnTe - 10 at % Bi after aging for 20 hrs (c) as quenched SnTe - 7 at % Bi (d) SnTe - 7 at % Bi after aging for 20 hrs.

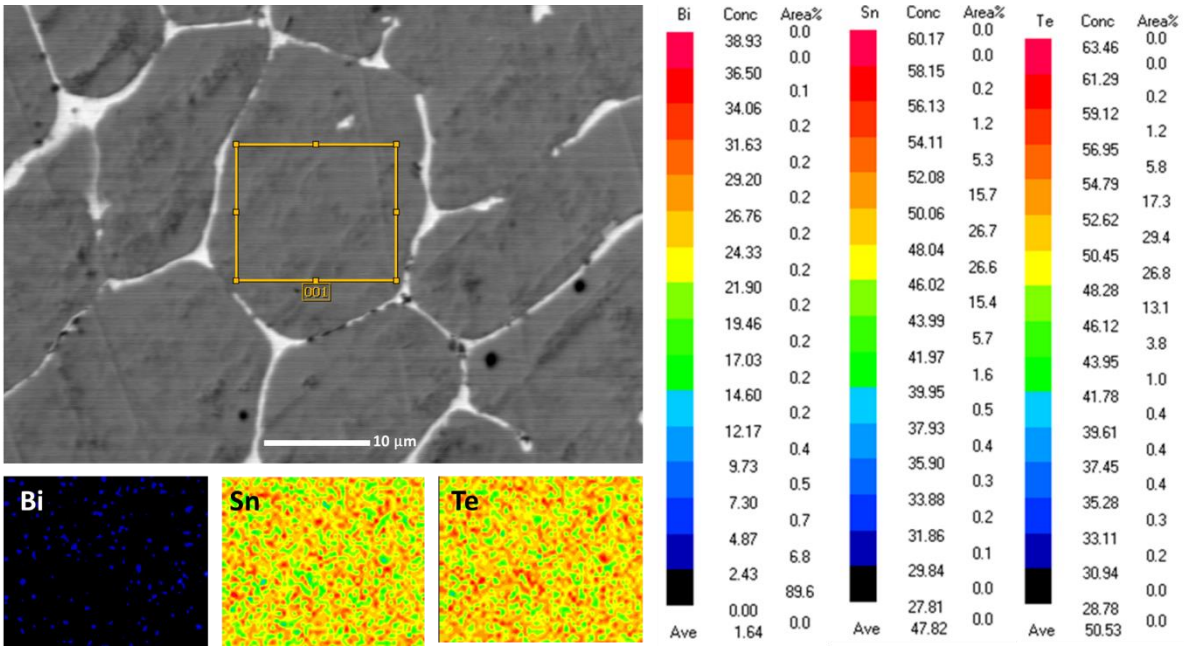

Figure 3.4: Elemental mapping of SnTe phase confirming the presence of Bi precipitate, for SnTe – 7 at % Bi as quenched sample. This analysis was conducted after determining the existing phases as shown in figure 3.3.

EPMA results show that there are two phases in the systems considered in this experiment. Since Bi has limited solubility in SnTe, it forms Bismuth secondary phase with a little amount of Sn and Te soluble in it. The majority of the phase were SnTe phase, which has some Bi doped in it. The fractions of the phases were consistent with the initial nominal composition of the samples. These phases are labeled in figure 3.3a. The solubility of the elements in each phase is tabulated in table 3.2. Unlike the reported solubility by Adouby et al. [14], the EPMA analysis shows that all the three samples have Bi as a secondary phase and the maximum solubility is limited to less than one at%. Since around one at%, Bi solubility is well studied by [12], and a high concentration of Bi will, most probably, cause loss of the semiconductor property.

Phases Present	Components	SB7	SB10
Bi Phase	Bi	99.19 ± 0.01	99.5 ± 2.1
	Sn	0.53 ± 0.2	0.4 ± 0.1
	Te	0.28 ± 0.04	0.08 ± 0.03
SnTe Phase	Bi	0.78 ± 0.02	1.5 ± 0.2
	Sn	48.27 ± 0.2	46.2 ± 1.6
	Te	50.94 ± 0.2	52.3 ± 1.8

Table 3.2: Bi solubility in SnTe phase, and Sn and Te in Bi phase.

The mechanical property of a material is usually related to the grain and particle size. In the presence of a secondary phase as the case of this work, it is the volumetric distribution of the second phase that modifies the mechanical property of the SnTe phase. It is shown in figure 3.3 that the Bi phase has a random distribution throughout the sample, and its structure/shape is also extremely irregular. Therefore it is convenient to study the effect of the Bi secondary phase regarding its volume fraction, rather than it is atomic/weight percent. The volume fraction calculated by ASTM procedure, specifically called Determining Volume Fraction by Systematic Manual Point Count [18], shows that the volume fraction of Bi has a direct relationship with its nominal concentration.

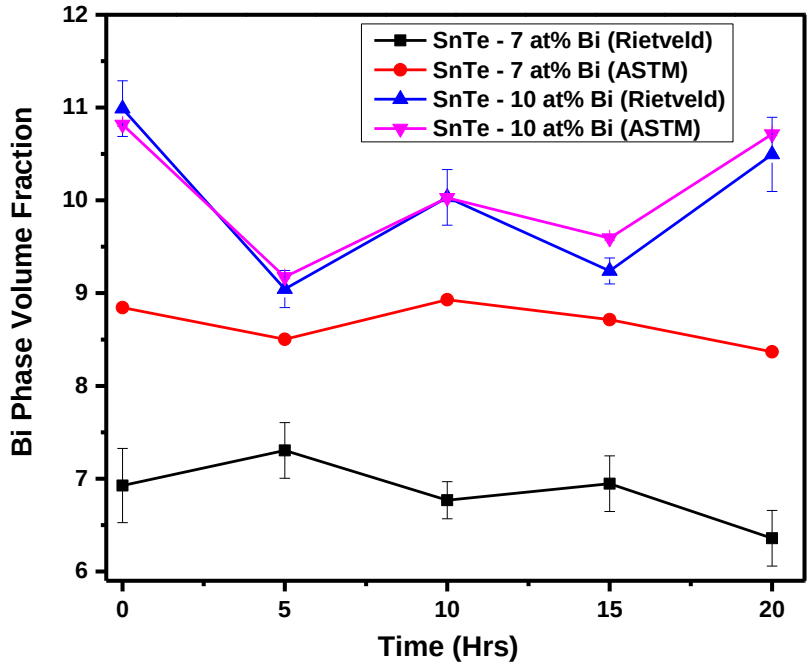

Figure 3.5: Bi phase volume fraction, obtained from Rietveld refinement and ASTM procedure, as a function of aging time. The value of 95% CI is so small that makes the error bar smaller than the symbol size used in the plot.

3.3.2 XRD Analysis

The XRD analysis of the samples is used to determine the phases presented in the samples; the fraction of the phases; lattice constant of the SnTe phase; the crystallite size SnTe phase and to check the change in lattice constant between pure SnTe and Bi-doped SnTe. The primary purpose of using XRD was to identify the phases present in the sample. The XRD analysis was essential to check whether Bi was fully soluble or not, especially for SB7. Indexed XRD pattern is presented in figure 3.6. It shows that a significant amount of Bi phase remained insoluble in SnTe. The fraction of the secondary phase Bi and that of SnTe was identified by quantitative phase analysis employed in Rietveld refinement technique. The Le Bail refinement was taken as a reference to check how good the whole pattern profile of the Rietveld refinement was. The main parameters refined in this analysis are scaling factor, lattice constants, profile parameters, preferred orientation

parameter, and atomic coordinates. Besides, isotropic thermal parameter, anisotropic thermal parameter and occupancy factor are refined according to the need of refining these parameters for the specific XRD pattern.

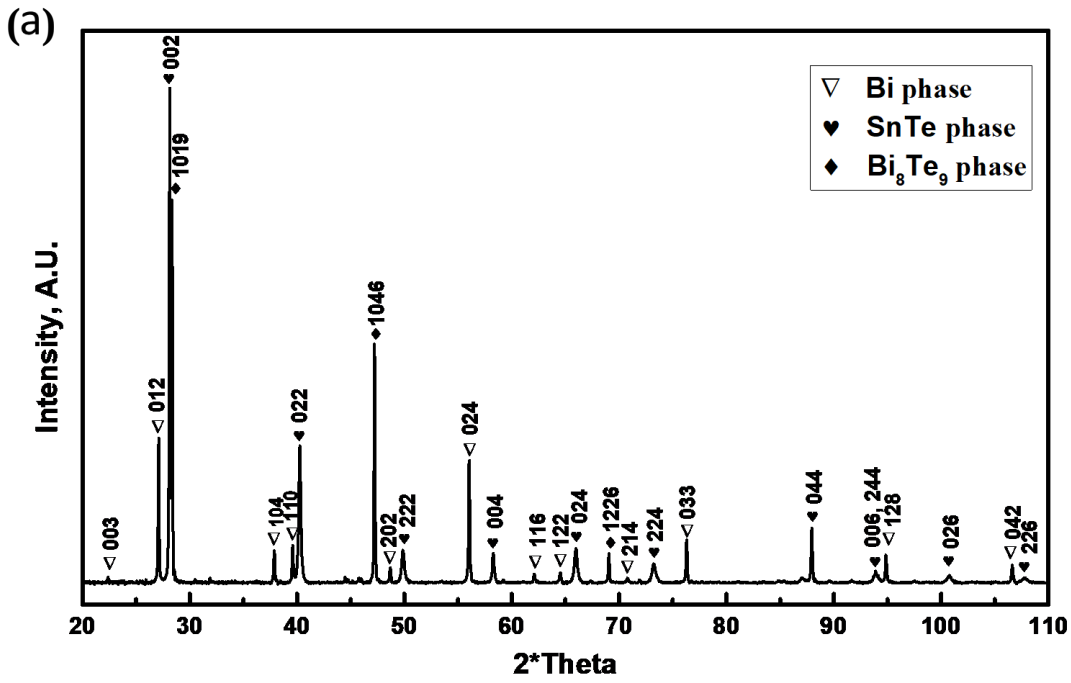

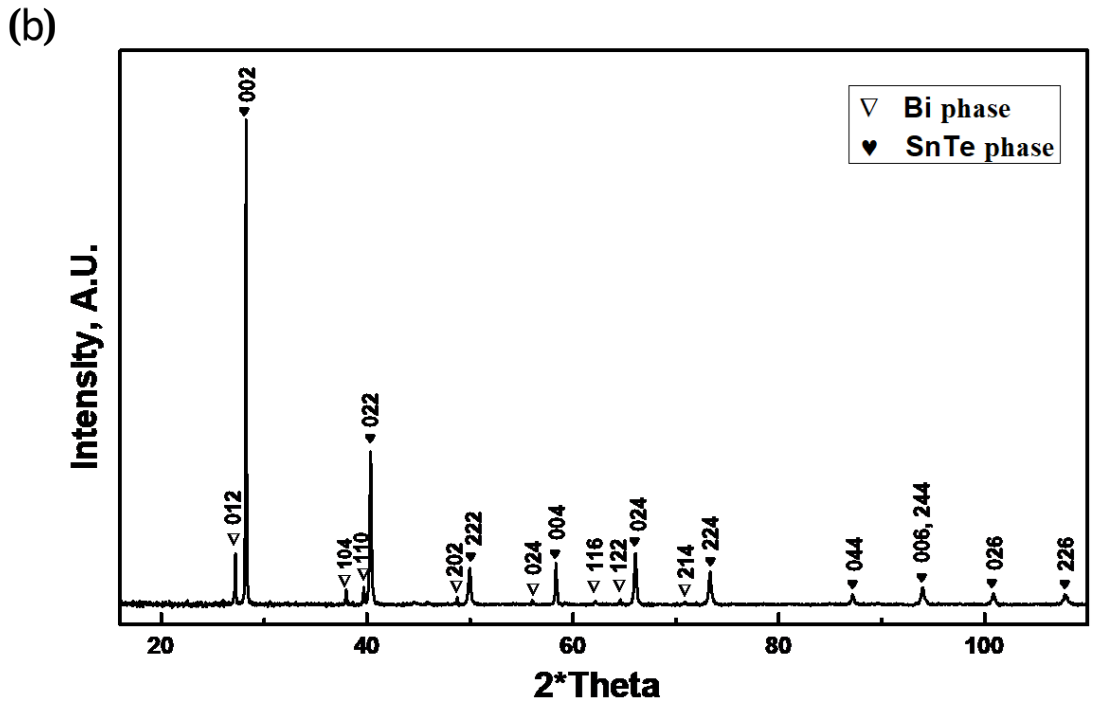

Figure 3.6: powder XRD pattern of (a) SnTe - 13 at % Bi, (b) SnTe - 7 at % Bi.

Unlike SB7 and SB10, which forms only two phases, SB13 results in the formation of the third compound that may be less important for the thermoelectric application, or make the study a bit complex. Therefore this study focusses on the compositions that have less Bi than 13 at %. The third compound may have a tiny fraction of the total sample, and that may be the reason for its absence in the SEM images. Otherwise, it may be an as bright phase as Bi phase, since it contains more amount of Bi than the Sn. The more the amount of Bi the brighter will be the color of the microstructure, as it was discussed in chapter 4.

3.3.3 Rietveld Refinement

The Rietveld refinement has been done by considering the possibility of the presence of Bi in SnTe. Accordingly, a Bi containing SnTe unit cell, $BiSn_3Te_4$, is taken as a reference from a standard database. This unit cell has a rock salt structure where Bi occupies some of the Sn lattice

points. The unit cell considered for Rietveld refinement is taken as a reference that will be modified during the refinement process. In this unit cell, it may seem that Bi substitutes 25% of the Sn. It is a miss leading representation that will serve as a reference to start the Rietveld refinement process. The Rietveld analysis refines the occupancy of this lattice point and tells the fraction of the lattice point occupied by each atom, which may be indicative of Bi solubility in SnTe. The occupancy of Bi varies with the duration of aging. This variable occupancy may be indicative of time-dependent diffusion of Bi during heat treatment. Actually, the solubility of Bi found to be very small, after refining the site occupancy of Bi.

Silicon powder standard sample was used for determining peak broadening due to instrumental error or sample preparation. In that the full width at half maximum (FWHM) obtained by using the Si standard was 0.09 degree 2θ for the (111) peak found at 28.4285 degree 2θ and varies with 2θ as a function of tanθ due to wavelength dispersion [22]. Assuming Si standard has negligible peak broadening, the obtained FWHM is taken as instrumental broadening. The instrumental parameters that were saved with the software, of PanAnalytical, was consistent with the instrumental broadening.

(a)

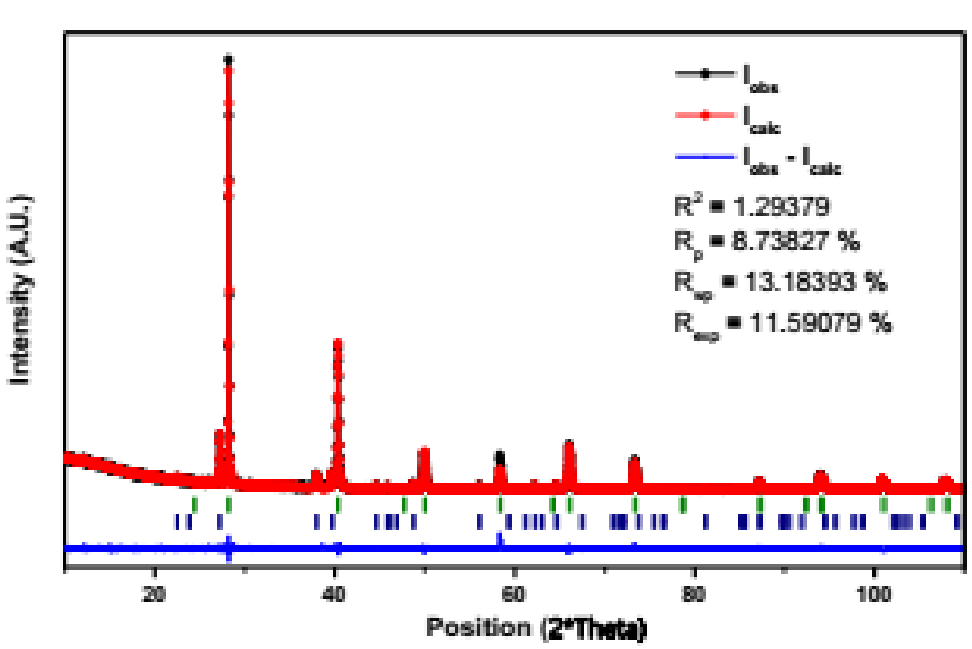

(b)

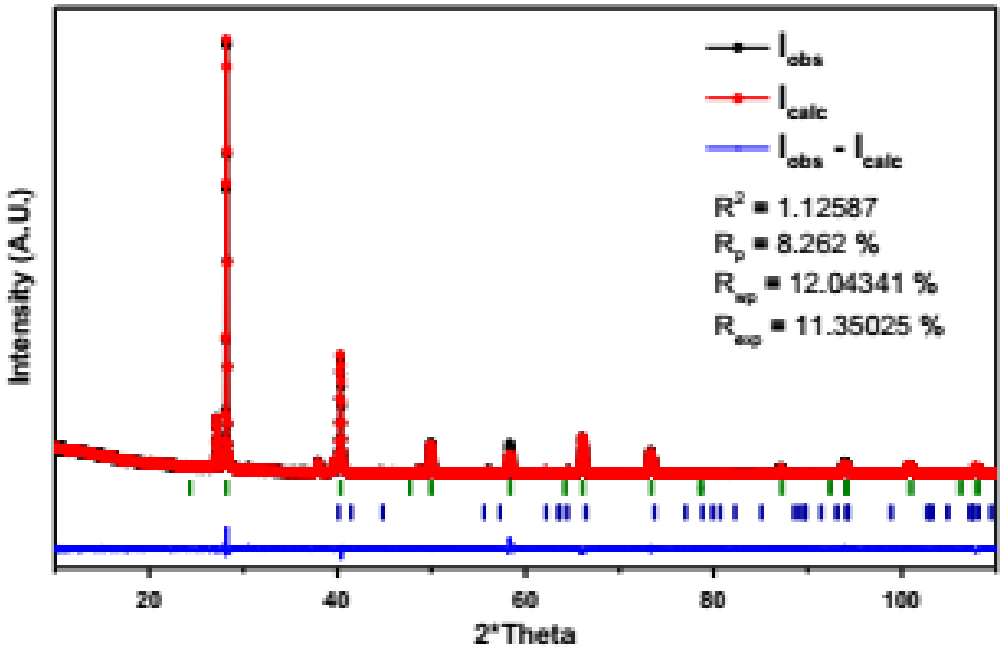

(c)

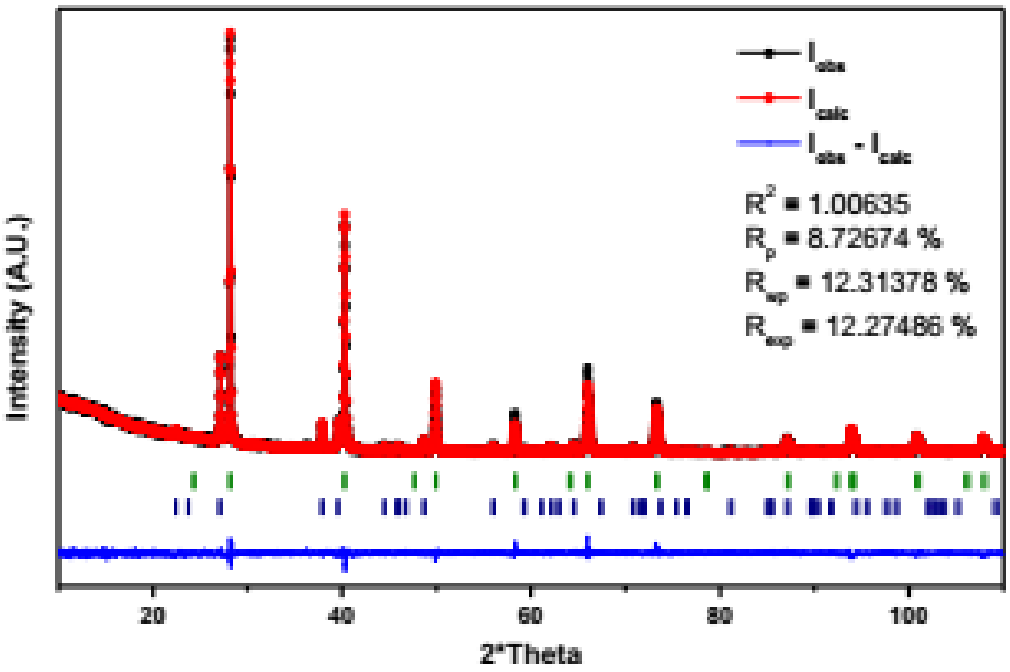

Figure 3.7: Whole profile pattern fitting by Rietveld refinement of (a) SnTe - 7 at % Bi, (b) SnTe - 7 at % Bi aged for 15 hrs. (c) SnTe - 10 at % Bi aged for 15 hrs.

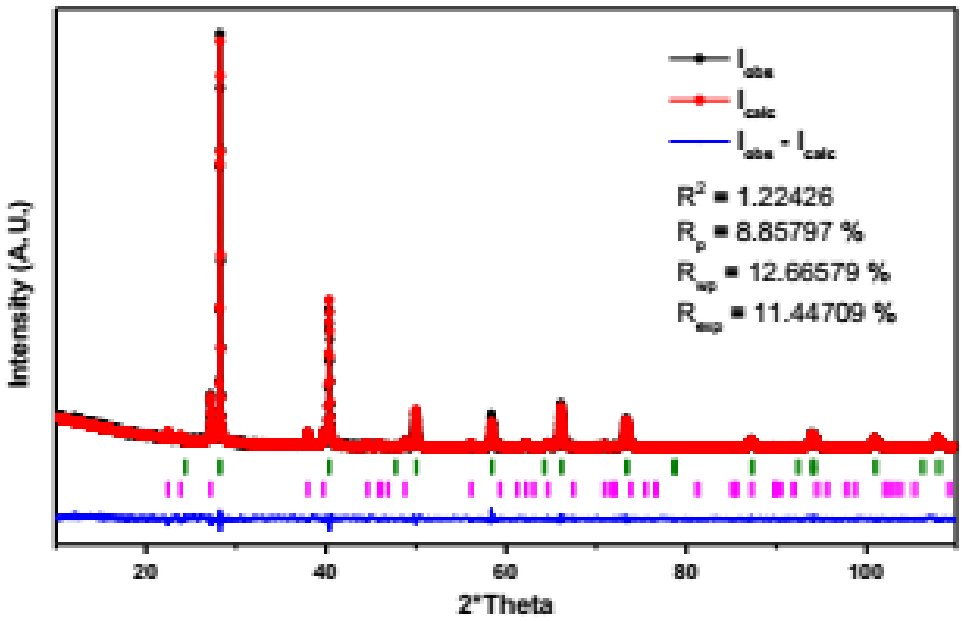

Figure 3.8: Whole profile pattern fitting by Le Bail refinement of SnTe - 7 at % Bi.

The procedure followed in this work is believed to cause relatively small strain. This effect is shown by the similarity of peak broadening of quenched and heat treated samples. Even after heat treatment, which can relieve strain, the peak broadening has similar behavior. Accordingly, it is assumed that the peak broadening is dominated by Lorentzian/Cauchy type. For this reason, profile fitting for Rietveld refinement is performed by considering Pearson VII method. The other merit of this method is its relatively low error in determining instrumental peak broadening after A. Monshi [23]. The broadening of a single diffraction peak is the product of the crystallite dimensions in the direction perpendicular to the planes that produced the diffraction peak [22].

The summarized result in table 5.1 shows that there is a variation of composition both with aging time and with Bi concentration. This implies that each of the phases have different composition which is dependent on both the nominal compositions and on the processing method. The refined site occupied factor indicates that there was a competition between Bi and Sn to occupy the 4a

Wyckoff position. This phenomenon is an indication of the formation of solid solution by the system, rather than forming compound.

3.3.3.1 The Crystallite Size and Microstrain

Once an alloy is formed, the XRD peaks will directly be due to the phases, which may contain one or more of the elements. The crystallite size depends on the extent of crystallinity of the corresponding phase so that each phase will have its crystallite size. To calculate the crystallite size of a given phase the peaks that correspond to the phase has been considered. The crystallite shape should not necessarily be spherical, i.e., different peaks of a given phase can result in different crystallite size (dimension of the crystallite corresponding to the diffraction plane). However, the average value will be taken to approximate it by spherical shape.

In order to identify the orientation and shape of the microstructure, crystallite size and shape were analyzed by using Hall-Williamson and Scherrer equations. Unlike the common expectation of nearly normal variation of Full Width at Half Maximum, FWHM, or the integral breadth with 2θ, it is found that only a few of the SnTe peaks have such variation. This variation has been reasoned out concerning the Rietveld refined preferred orientation, which gives the direction of the preferred orientation of the crystallite of the powdered sample. This analysis was helpful in determining the range of crystallinity which has some impact on the electrical conductivity and phonon scattering by the crystal lattice. Figure 3.9 shows the W-H plot of some of the samples analyzed by this method.

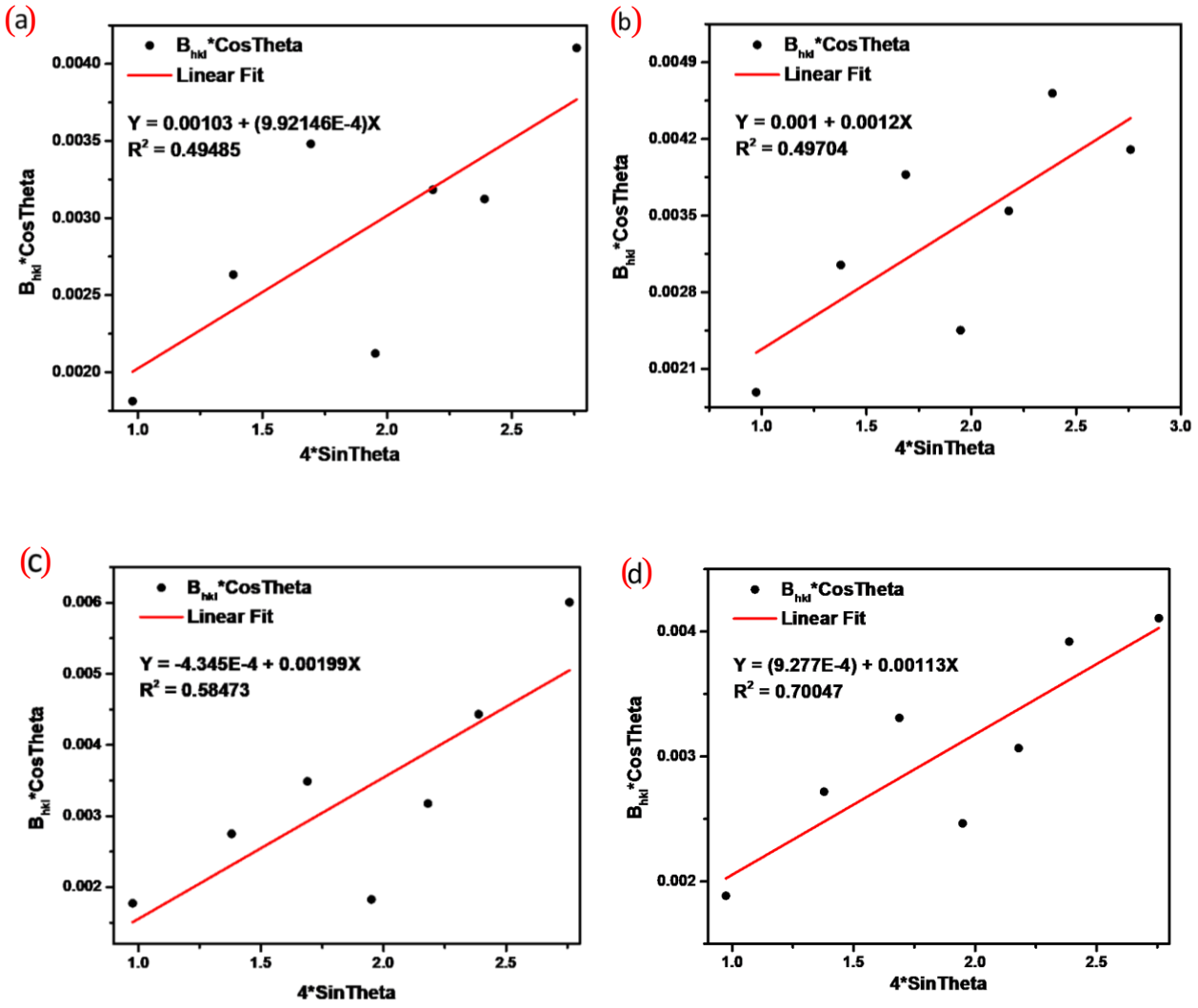

Figure 3.9: Williamson-Hall plots (a) SnTe – 7 at % Bi aged for 5 hrs, (b) SnTe – 7 at % Bi aged for 20 hrs, (c) SnTe – 10 at % Bi as Quenched, (d) SnTe – 10 at % Bi aged for 20 hrs.

In all XRD analysis, it is found that the observed (004) peak of SnTe phase has more intense peak than the calculated one. Even though the difference is not as significant as (004) plane, similar phenomena are observed for (002) plane. This difference is consistent with the preferred orientation found by Rietveld refinement, (001). The effect of preferred orientation is also shown in the plot of Scherrer and Williamson-Hall equations as shown in figure 3.9, where the diffraction peaks corresponding to these planes have lower FWHM than the other peaks. This smaller FWHM

indicates that the crystallite dimension perpendicular to the plane of preferred orientation is longer than the other dimensions. It also may be the reason for lack of goodness of fit of the linear fit.

3.3.4 Thermoelectric Properties

The thermoelectric property of SnTe is more of the result of its high vacancy concentration in the Sn lattice site. The presence of these vacancies makes it a p-type thermoelectric material. With the addition of Bi, it is possible to modify this nature of SnTe. Hence there is some number of possibilities about the lattice site of the Bi dopant in the SnTe phase. Bi can be doped in the vacant site of the Sn lattice, or it can substitute the Sn. In either case, Bi will reside in the Sn lattice, as it is discussed in the next section.

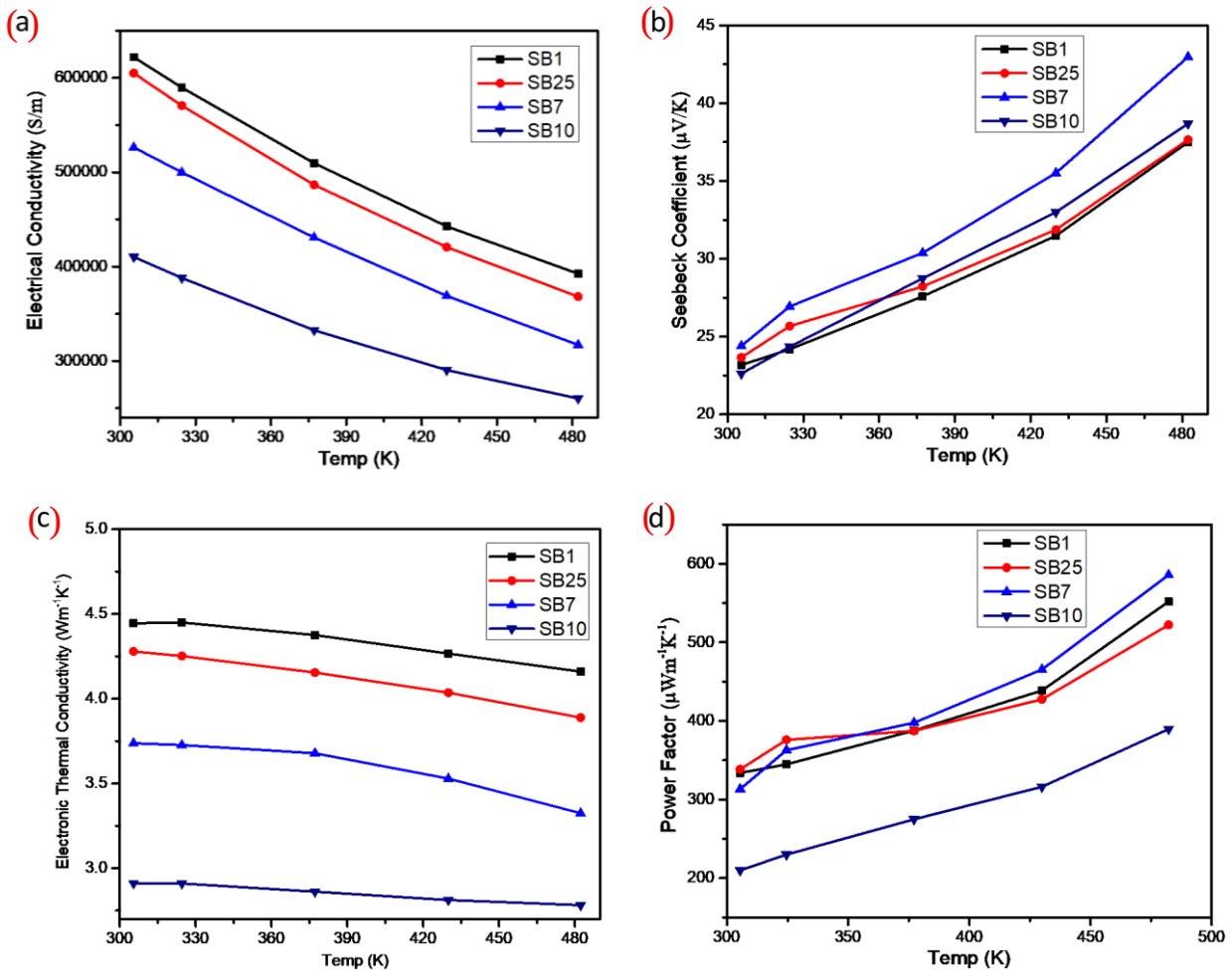

Figure 3.10: Thermoelectric properties of the as-quenched samples. (a) Electrical conductivity (b) Seebeck coefficient (c) Electronic thermal conductivity (d) Power factor.

Figure 3.10a shows that electrical conductivity decreases with increasing Bi concentration. This property is more noticeable when Bi concentration changes from 2.5 at% Bi to 10 at% Bi. On the other hand, the electrical conductivity decreases with increasing temperature. The power factor versus temperature plot shows the combined effect of electrical conductivity and Seebeck coefficient. The effect of the Seebeck coefficient is observed more than that of the electrical conductivity when the power factor is analyzed as a function of temperature. The power factor increases with temperature similarly as the Seebeck coefficient. Except for SB10, all the samples

have nearly the same power factor. It looks like the effect of a relatively low value of electrical conductivity is affecting the power factor, which is smaller than the other values. Both electrical conductivity and electronic thermal conductivity have distinctly different values for the different composition. The low thermal conductive property of Bi semi-metal observed on the decreasing value of electronic thermal conductivity with increasing Bismuth concentration. The hot-pressed samples also have similar nature of thermoelectric properties as shown in figure 3.11.

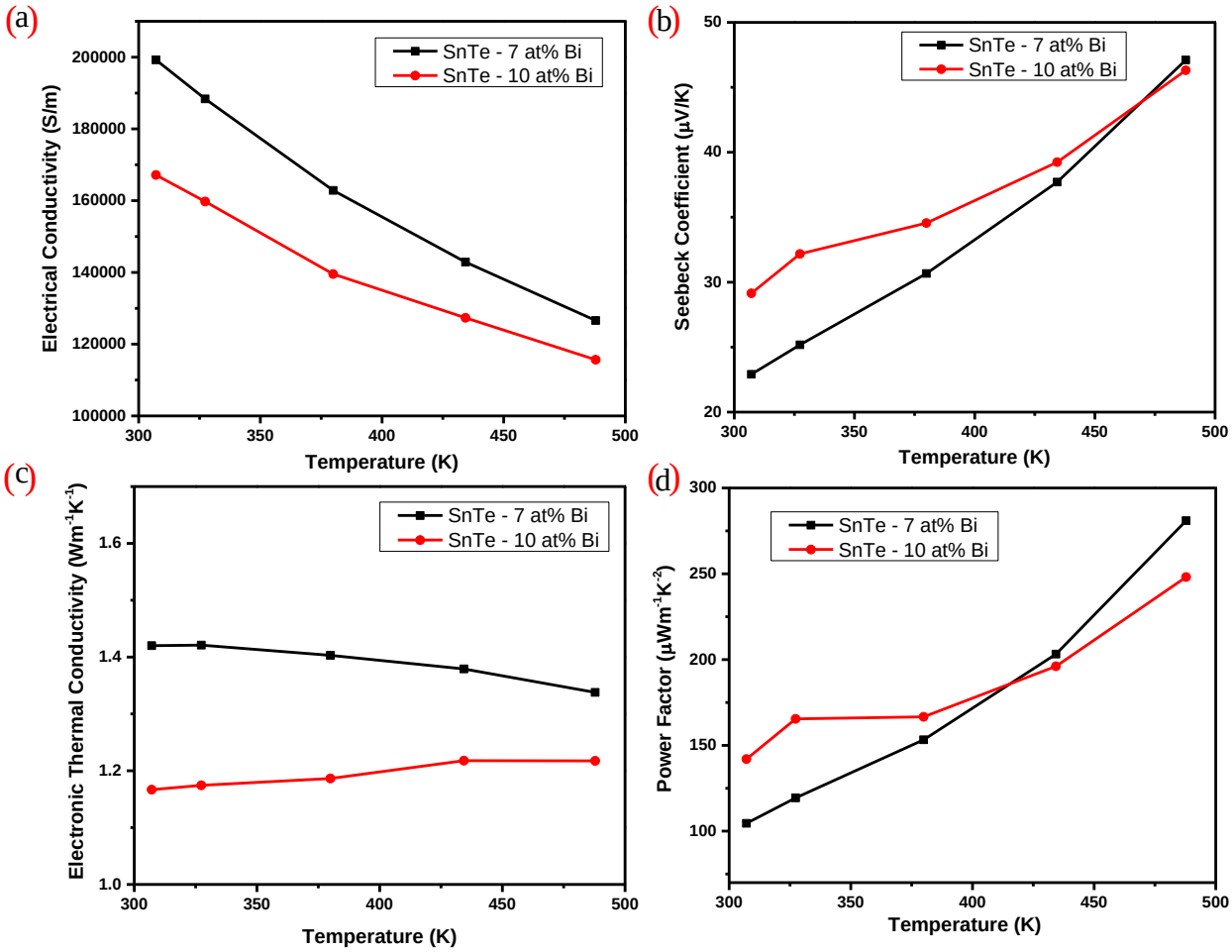

Figure 3.11: Thermoelectric properties of the hot-pressed samples. (a) Electrical conductivity (b) Seebeck coefficient (c) Electronic thermal conductivity (d) Power factor.

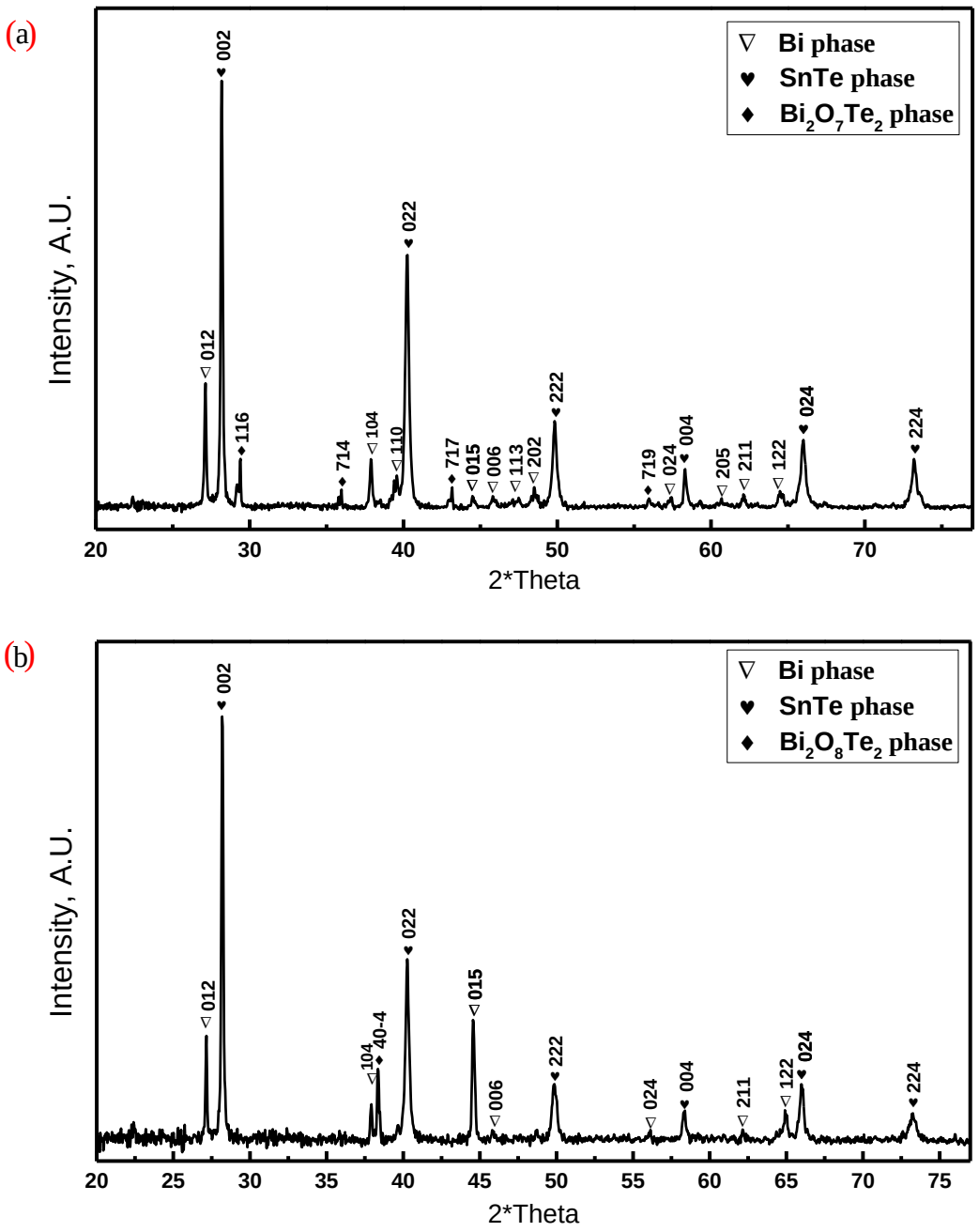

Figure 3.12: XRD pattern of (a) SnTe - 7 at % Bi, (b) SnTe - 10 at % Bi, after hot-pressing.

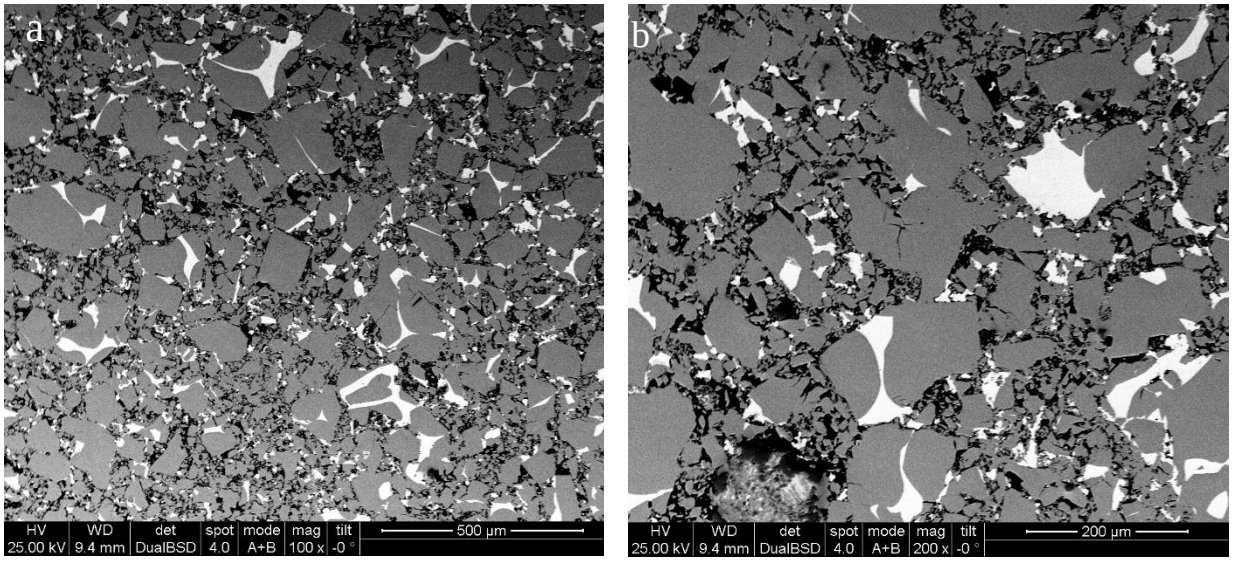

Figure 3.13: Microstructure of the hot-pressed sample. (a) SnTe – 7 at % Bi. (b) SnTe – 10 at % Bi.

The XRD image of the hot-pressed sample shows that there was a possibility of contamination of the sample during the hot pressing procedure. This is anticipated from the presence of some oxide peaks. On the other hand it can be clearly seen from the EPMA image of the hot pressed sample that the selected temperature and pressure for the hot-pressing procedure may need some more optimization, assuming that the phase diagram reported by Adouby it al. [14] has no error. The need for more optimization was shown by 86.0 and 85.5 % compaction, resulted in this work. The lack of thermoelectric property of the hot-pressed sample compared to the ingot may be due to this lack of compaction or the presence of oxidation during the process.

3.3.5 Mechanical Properties

The result of the aging curve, figure 3.12, implies that both homogenization and aging increase the Vickers hardness, HV, of the material. The original idea of introducing homogenization was to increase the solubility of Bi in SnTe phase. Even though the homogenization time was longer than that of aging the improvement in the corresponding HV during homogenization was smaller. The homogenization takes place at the eutectic temperature, to be sure that no eutectic microstructure remains in the sample. The maximum value of HV observed at about 10 hrs and 15 hrs for SB7 and SB10, respectively. In this work, the aging processes stopped when over aging had been observed, after reaching the maximum HV. It is evident that HV has an inverse relationship to the concentration of the Bi. This relationship is observed from the higher HV value of SB7 than that of SB10, throughout the heat treatment processes.

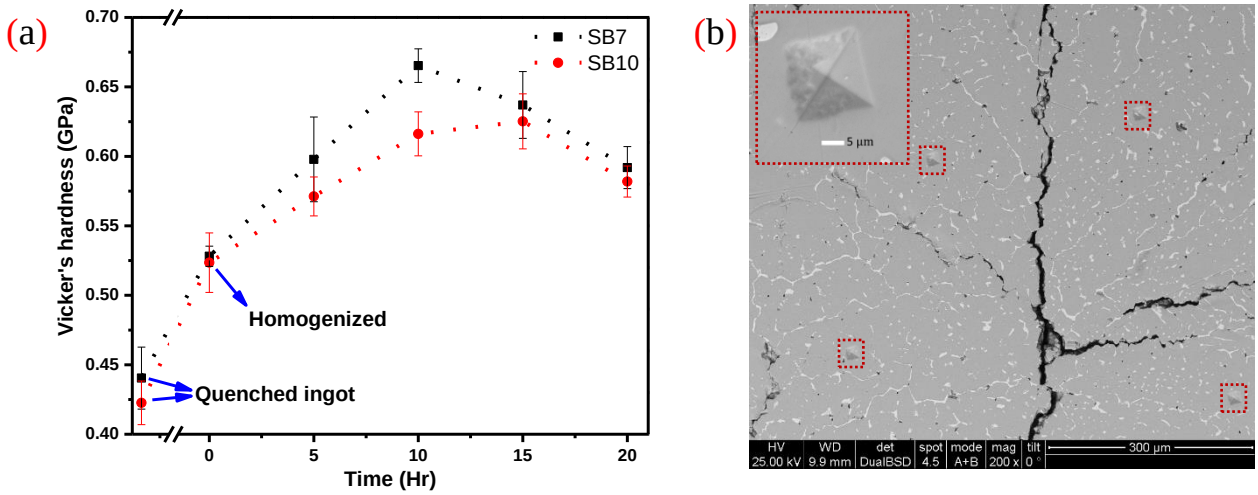

Figure 3.14: (a) Aging curve. The broken lines of the x-axis is introduced to refer to the time spend during homogenization. (b) EPMA image of the indented microstructure showing the randomly selected spots for indentation were far enough with each other. The inset shows the shape of a particular indentation with a diamond shape. Since the HV test is characteristic of the region only around the indentation, the observed cracks have no effect on the measurement

3.4 Discussion

3.4.1 Bi Solubility in SnTe and Its Effect on Thermoelectric Property

Different researchers found the different amount of solubility of Bi in SnTe. Typical of them are; 13.29 at% by Chiu et al [24], about 4 at% by Zhiwei et al [10], 10 at% by Adouby et al [14], less than 1 at% by D. M. Freik et al [12], and M. A. Tamor et al [25]. The conclusion of Chiu et al. achieved by taking composition in the SnTe-Bi_2Te_3 pseudo-binary region, which will have a high probability to get non-rock salt structure; instead, it will form a rhombohedral structure with various layers of Sn, Te, and Bi. Therefore it is difficult to consider this as the solubility of Bi in SnTe.

On the other hand, a pure bismuth phase is found in the work of D. M. Freick et al. by taking one at% of Bi. Compared to Freik et al. the work of Zhiwei et al. is indicative of the possibility of finding more solubility of Bi in SnTe by managing the working condition. But compared to the absence of this phase in the work of Zhiwei et al by taking 2 and 4 at% of Bi, the lack of solubility expressed by presence of Bi phase in the work of Freik et al may be either due to the improper working condition or due to the larger atomic radii of Bi than that of Sn and Te, or the interstitial site. This same reason may be right for the lack of solubility of Bi in SnTe phase, in this work.

According to the work of Zhiwei et al., ZT will increase with increasing solubility of Bi, and an increasing amount of Bi precipitate, but it decreases with increasing Bi secondary phase. Therefore increasing the solubility of Bi in SnTe will help to shift the existence of Bi precipitate and Bi secondary phase from 4 at% and six at% Bi, respectively, to 10 at% and 12 at%. There will be similar effects on the concentration and mobility of charge carriers, which shall be studied together with other thermoelectric properties.

3.4.2 Bi Solubility and Change in Lattice Constant of SnTe

The result of Rietveld analysis, shown in table 5.1, indicates that the solubility of Bismuth varies for every system and there was no specific composition for the gray phase. Besides, the crystal structure of the solvent was preserved upon addition of the solute. These facts implies that the Bi dissolved in SnTe is a solid solution system. Since there were no specific compound founded from the XRD analysis, the system can hardly form a compound for the compositions considered in this work in similar working conditions. The lattice constant of the solvent varies with the addition of the solute but this doesn't affect the crystal structure of the solvent.

According to Zhiwei et al. [10], the lattice constant of Bi doped SnTe increases with increasing Bi concentration, even more than 4 at% of Bi. If the maximum solubility of Bi were only 4 at% the change in lattice constant after 4 at%, Bi would be negligible. The observed small change in lattice constant after 4 at% Bi shows the possibility of more solubility of Bi, in the corresponding working condition. While calculating the lattice constant, only the amount of Bi dissolved in SnTe might have to be considered. However, Zhiwei et al. might have considered as if all the 6% and 8% Bi dissolved in the lattice of SnTe, in the sketch of lattice constant vs. Bi concentration. This kind of consideration may be one reason for why the sketch is curved and deviate much from Vegard's law; since a more significant change in Bi concentration than the reality corresponds to the small change in lattice constant causes decrease in the slop of the graph. Otherwise, both deviation from Vegard's law and error in considering Bi solubility might include. Therefore determining the amount of Bi dissolved into the unit cell by taking point analysis (under EPMA) may be one way to find the effective concentration of Bi that causes the change in lattice constant, Bi dissolving in the crystal of SnTe.

The solubility of Bi in SnTe, founded by EPMA, may have some error due to lack of capability differentiating Bi dissolved in SnTe from Bi precipitate. Since the size of the electron beam is 1 to 2 microns, the WDS point analysis can detect SnTe crystallite, and Bi precipitate altogether. This limited solubility is more probable since the peak shift, which is sensitive to the dissolved Bi and hence the change in lattice constant rather than Bi precipitate, of the XRD of the samples, was not significant.

On the other hand, the solubility also may be dependent on how the stoichiometry took. According to Zhiwei et al. [10], Bi is taken to substitute Sn, i.e., $Sn_{1-x}Bi_xTe$. However, in this work, Bi is taken to substitute either Sn or Te, i.e., Bi: SnTe. The similar factor may be right in the work of Freik et al. in other words, Tamor et al., similar to this work, take the composition along the line from SnTe to Bi, in the ternary phase diagram. Whereas Zhiwei et al. take the composition along the line from SnTe to BiTe. If the composition vs. temperature phase diagram generated for the latter case, there may be a high probability to obtain high solubility of Bi in SnTe, since the stoichiometry taken in such a way that Bi will substitute Sn. It may be out of this high solubility that Zhiwei et al. found about 4 at% Bi solubility. If this is true homogenization and then aging will give a better amount of precipitate. If not (if the solubility is less than 10 at %), it will be good to anticipate more solubility of Bi along SnTe to Bi too. Besides, Zhiwei et al. [10] was able to measure TE properties up to 600 ℃. This range of temperature implies that the corresponding composition has a higher melting point (or the solvus line) than 600 ℃.

Unlike the reported solubility by Adouby et al. [14], the EPMA analysis shows that all the three samples have Bi as a secondary phase and the maximum solubility is limited to less than 1 at%. Since around 1 at%, Bi solubility is well studied by [12], and high concentration of Bi will, most probably, cause loss of the semiconductor property, this research mainly focused on the 7 at% and

10 at% Bi systems. After analyzing the two samples, some more samples considered from less Bi concentration side. The target of the last samples to both approve the anomalous solubility compared to Adouby et al., and to consider the compositions for thermoelectric property measurements. Both the observed thermoelectric properties and the solubility of Bi for the latter samples were consistent with the former once.

3.4.3 Volume Fraction of the Phases

The SEM image, shown in figure 3.3, indicates that the Bi phase in the as-quenched sample is long and randomly distributed. It seems it has been expelled from the SnTe phase since SnTe phase solidified at a higher temperature than the solidification temperature of Bi. As a result, Bi solidification takes place around the grain boundary of the SnTe phase. This kind of solidification may be the reason for the observed shape of the Bi phase. With aging, most of the long Bi phase microstructure changed into pieces. This change can be due to the diffusion of Bi into the SnTe phase near the Bi-SnTe phase boundary. However, there has not been detected an increase in Bi solubility by WDS point analysis, nor by the corresponding XRD. This lack of solubility indicates that the diffused Bi into the SnTe phase has formed precipitates and restricted to the phase boundary of the SnTe phase. The precipitates have not been distributed uniformly in SnTe phase. Were it has been distributed it would be detected by WDS point analysis which has been taken far enough away from the phase boundary, to prevent drifting of the beam to the Bi phase. In order to further investigate this, the fraction of the two phases in each sample have been calculated by two methods. First, Rietveld refinement of the XRD pattern gives the weight fraction of each of the phases. Second, using the ASTM procedure, from which the volume fraction can be calculated.

XRD is more of dependent on the crystal structure of the sample. Accordingly, the relative intensity of the peaks directly gives information about the volume fraction of the different phases of the sample. Based on the information of the crystal structure, the theoretical density will help to convert the volume fraction to weight fraction. This method is less sensitive for detecting the change in mass when a solvent atom was substituting the solute atom, during solid solution, unless the corresponding site occupancy is refined. For instance, when Bi in SnTe –Bi system substitutes Sn, practically, the molar mass of the SnTe phase will be changed due to the difference in molar mass of Sn and Bi. This also causes a small increase in unit cell volume. These have a different effect on the density of the phase. However, since XRD is less sensitive to the molar mass of the atoms, almost only the change in volume will be considered in the determination of theoretical density. This problem affects the accuracy of the weight fraction of the different phases analyzed by Rietveld refinement. As a result, there may be some difference between the weight fractions calculated by Rietveld analysis and other methods, such as by analyzing the SEM image of the phases.

During the Rietveld refinement, the calculated density of the two phases was varied with the site occupancy factor of Bi dopant. This may indicate that the change in mass of the unit cell with Bi dopant and also the corresponding change in volume might have been considered within the calculated value of the density. If this is the case, the volume fraction founded by Rietveld refinement is more reliable than that of the other method, recommended by ASTM. This is true only from the perspective of the accuracy of the calculated density. On the other hand, the volume fraction obtained by Rietveld refinement might have some other errors due to the detection of Bi precipitate. According to Zhou et al. [10], the Bi phase retains its crystal structure while forming a precipitate in SnTe phase. These precipitates were not detected by electron microscopy so that

the volume fraction calculated from the images did not include Bi precipitate with Bi secondary phase. Since Bi precipitate and Bi secondary phase have the same crystal structure, both can be detected by the X-Ray diffractometer. Such differences may be the reason for the difference in volume fraction calculated by the two methods, especially for SnTe - 7 at % Bi.

3.4.4 The effect of Bi on Mechanical Property of the System

Unlike the solubility limit suggested by Adouby et al. [14], the composition is chosen in this experiment lies beyond the solubility limit, in the spinodal decomposition region. Therefore the possible nucleation mechanism of Bi precipitate is homogeneous nucleation, heterogeneous nucleation or spinodal decomposition. Since the first solubility of Bi is not significant, the spinodal decomposition can hardly take place. In this region, there is less barrier against the other nucleation mechanisms.

After reaching maximum label of hardening the prolonged aging results in softening of the material, which is the so-called over-aging. Having been quenched (i.e., high undercooling) from high temperature during the sample preparation, the sample contains mostly fine particles. During aging, the relatively larger particles grow while the relatively smaller ones dissociate. The maximum hardness corresponds to the presence of an optimum number of small and large particles [26]. This kind of age hardening takes place irrespective of the number of phases present in the sample. However, the change in the microstructure of the phases with increasing aging time is indicative of the diffusion of Bi atoms into SnTe phase. Therefore the observed improvement in the hardness of the material is the combined effect of both Bi precipitate in SnTe phase and aging of the SnTe phase itself. The observed increase in hardness in a relatively short time may be due

to the existence of heterogeneous nucleation, which is energetically preferable, as a dominant mechanism. Vacancy supersaturation may be the other reason.

The most important results of the present investigation are the possibility of production of thermoelectric material with the improved mechanical property. Since the electronic property of the thermoelectric material depends mainly on the crystal structure and the concentration of the soluble dopant, which shows no change with aging, it is assumed that it will remain the same after aging. Hence the aging heat treatment may be changing only the mechanical property of the material. It is essential to do some more experiments to conclude in this way. The smaller HV improvement during homogenization than that of during aging may be an indicator of the reasonability of the selected homogenization temperature.

$$\sigma_y = \sigma_0 + k_y d^{-1/2} \qquad 3.1$$

It can hardly be anticipated that the observed improvement in the mechanical property is due to the presence of precipitates since the volume fraction of the Bi phase measured by analyzing the SEM image did not change significantly. It shows more (or comparable) value than that obtained by Rietveld refinement. Rather the aging curve can be due to the change in grain size of the system. This may also be the reason for the observed change in the structure of the Bi phase. As it is described by the Hall-Petch equation (equation 3.1), the Vickers' hardness (hence the strength) increases with decreasing average grain size, but only for some range of values of the grain sizes. The improved value of the hardness is the result of the optimum amount of coarse and fine grains.

3.4.5 The Effect of Bi on Thermoelectric Property of the System

Since Bi has one more electron than Sn, it can minimize the hole concentration of the SnTe system. Its larger radii than the Te and its valence electronic state does not allow it to substitute Te, or this will be energetically unfavorable. The most likely lattice sites for Bi dopant are the lattice sites of Sn. This can be either by substituting the existing Sn or by filling the vacancy left by Sn. These two possibilities are stated in the following defect equations. For a system that naturally has enough vacancy, it may be energetically unfavorable for Bi to substitute Sn. Therefore the first of the two possible defect equations seems the most probable process of Bi doping mechanism. This may be the reason for the observed decrease in electrical conductivity with increase in Bi content from 2.5 to 10 at%. There also may be concentration dependent diffusion of Bi [12] into SnTe, in which the amount of secondary phase Bi will affect its solubility. The hysteresis observed in the thermoelectric property measurement also may be indicative of the stability of the material.

$$Bi + Sn_v^{6\cdot} \rightarrow Bi_{Sn}^{\cdot} \qquad 3.2a$$

$$Bi + Sn_{Sn}^{\cdot\cdot} \rightarrow Bi_{Sn}^{\cdot} \qquad 3.2b$$

3.4.6 Relationship among Microstructure, Mechanical and Thermoelectric Properties

The improved mechanical property with an insignificant effect on the lattice constant is an indication of not only good mechanical property but also the stability of the material. On the other hand, the Seebeck coefficient hysteresis curve has a small area. Therefore it may be possible to get this material so stable that will not change its thermoelectric figure of merit after a long time of application. This will solve one of the problems of thermoelectric materials, i.e., loss of figure of merit of the material with a longtime application which can also be considered as heat treating the material with varying temperature.

The uniform distribution of the Bi phase, which has non-regular structure, may be one reason for the improved mechanical property. On the other hand the aging process enables to modify the microstructure of the phases, as shown in figure 3.3. The microstructure which has been modified by the aging process have different mechanical property than before aging. Consequently, it also result in different mechanical property than the as-quenched ingot. In that, it was able to afford to resist a more than 0.60 GPa load after aging for 15 hours. In addition the hot pressing process results in similar microstructure but with different distribution of the grain boundaries. The result of this modification was observed in the corresponding thermoelectric properties measured. The main advantage of the hot prosing process was observed in decreasing the electronic contribution to thermal conductivity. In general the processes followed in this experiment, i.e. quenching of the molten alloy, hot-pressing, aging and homogenization, results in the creation of different microstructure. In addition the different microstructure obtained are responsible for the observed mechanical and thermoelectric properties. Finally, incredible performances were obtained in terms of minimizing the electronic contribution to phono propagation, and increasing the mechanical property, Vickers's hardness, of the material.

3.5 Conclusion

This experiment was compared with other reports mentioned in the previous sections. The overall results enable to give the following conclusions:

- ✓ The solubility of Bi in SnTe has to be rechecked with the different working environment and characterization techniques.
- ✓ The nature and distribution of the Bi precipitate need to be characterized by advanced techniques.

- ✓ It may be advantageous to determine the nature of the phase boundary both between Bi precipitate and SnTe and between Bi secondary phase and SnTe.
- ✓ The mechanical property of the system can be improved in the presence of Bi dopant and Bi secondary phase.
- ✓ The aging heat treatment can improve not only the Vickers hardness but also it may increase the ductility of the material.
- ✓ It can hardly be concluded that the observed improvement in a mechanical property is due to the presence of precipitates since the volume fraction of the Bi phase measured by analyzing the SEM image did not change significantly. It shows more (or comparable) value than that obtained by Rietveld refinement.
- ✓ The electrical conductivity decreases both with an increase in Bi content and with an increase in temperature. The decrease in electrical conductivity may be due to the decrease in hole concentration as due to doping of Bi at the intrinsic vacancy of SnTe.
- ✓ The low thermal conductivity property of Bi semi-metal is observed on the decreasing value of electronic thermal conductivity with increasing bismuth concentration.

3.6 Reference

1. Femi, O.E., K. Akkiraju, B.S. Murthy, N. Ravishankar, and K. Chattopadhyay, *Effect of processing route on the bipolar contribution to the thermoelectric properties of n-type eutectic Bi22.5Sb7.5Te70 alloy.* Journal of Alloys and Compounds, 2016. **682**: p. 791-798.
2. Zhao, L.-D., S. Hao, S.-H. Lo, C.-I. Wu, X. Zhou, Y. Lee, H. Li, K. Biswas, T.P. Hogan, C. Uher, C. Wolverton, V.P. Dravid, and M.G. Kanatzidis, *High Thermoelectric Performance via Hierarchical Compositionally Alloyed Nanostructures.* Journal of the American Chemical Society, 2013. **135**(19): p. 7364-7370.
3. Park, J.G. and Y.H. Lee, *High thermoelectric performance of Bi-Te alloy: Defect engineering strategy*. Current Applied Physics, 2016. **16**(9): p. 1202-1215.
4. Banik, A., U.S. Shenoy, S. Saha, U.V. Waghmare, and K. Biswas, *High Power Factor and Enhanced Thermoelectric Performance of SnTe-AgInTe2: Synergistic Effect of Resonance Level and Valence Band Convergence.* Journal of the American Chemical Society, 2016. **138**(39): p. 13068-13075.
5. Bhat, D.K. and S. Shenoy U, *High Thermoelectric Performance of Co-Doped Tin Telluride Due to Synergistic Effect of Magnesium and Indium.* The Journal of Physical Chemistry C, 2017. **121**(13): p. 7123-7130.
6. Tan, G., F. Shi, S. Hao, H. Chi, T.P. Bailey, L.-D. Zhao, C. Uher, C. Wolverton, V.P. Dravid, and M.G. Kanatzidis, *Valence Band Modification and High Thermoelectric Performance in SnTe Heavily Alloyed with MnTe.* Journal of the American Chemical Society, 2015. **137**(35): p. 11507-11516.
7. Tan, G., L.-D. Zhao, F. Shi, J.W. Doak, S.-H. Lo, H. Sun, C. Wolverton, V.P. Dravid, C. Uher, and M.G. Kanatzidis, *High Thermoelectric Performance of p-Type SnTe via a Synergistic Band Engineering and Nanostructuring Approach.* Journal of the American Chemical Society, 2014. **136**(19): p. 7006-7017.
8. Al Rahal Al Orabi, R., N.A. Mecholsky, J. Hwang, W. Kim, J.-S. Rhyee, D. Wee, and M. Fornari, *Band Degeneracy, Low Thermal Conductivity, and High Thermoelectric Figure of Merit in SnTe–CaTe Alloys.* Chemistry of Materials, 2016. **28**(1): p. 376-384.
9. Tan, X., G. Liu, J. Xu, X. Tan, H. Shao, H. Hu, H. Jiang, Y. Lu, and J. Jiang, *Thermoelectric properties of In-Hg co-doping in SnTe: Energy band engineering.* Journal of Materiomics, 2018. **4**(1): p. 62-67.

10. Zhou, Z., J. Yang, Q. Jiang, Y. Luo, D. Zhang, Y. Ren, X. He, and J. Xin, *Multiple effects of Bi doping in enhancing the thermoelectric properties of SnTe.* Journal of Materials Chemistry A, 2016. **4**(34): p. 13171-13175.
11. Puneet, P., R. Podila, M. Karakaya, S. Zhu, J. He, T.M. Tritt, M.S. Dresselhaus, and A.M. Rao, *Preferential Scattering by Interfacial Charged Defects for Enhanced Thermoelectric Performance in Few-layered n-type Bi2Te3.* Scientific Reports, 2013. **3**: p. 3212.
12. Freik, D.M., S.I. Mudryi, I. Gorichok, V. Prokopiv, O. Matkivsky, I.O. Arsenjuk, O.S. Krynytsky, and V.M. Bojchyk, *Thermoelectric Properties of Bismuth-Doped Tin Telluride SnTe:Bi*. Vol. 61. 2016. 155-159.
13. Rogacheva, E.I., *The problem of doping of non-stoichiometric phases.* Journal of Physics and Chemistry of Solids, 2008. **69**(2): p. 259-268.
14. Adouby, K., A. Abba Touré, G. Kra, J. Olivier-Fourcade, J.-C. Jumas, and C. Perez Vicente, *Phase diagram and local environment of Sn and Te: SnTeBi and SnTeBi2Te3 systems.* Comptes Rendus de l'Académie des Sciences - Series IIC - Chemistry, 2000. **3**(1): p. 51-58.
15. Morelli, D.T., V. Jovovic, and J.P. Heremans, *Intrinsically Minimal Thermal Conductivity in Cubic $\mathrm{I}\mathrm{\text{\ensuremath{-}}}\mathrm{V}\mathrm{\text{\ensuremath{-}}}{\mathrm{VI}}_{2}$ Semiconductors.* Physical Review Letters, 2008. **101**(3): p. 035901.
16. Ioffe, A.F., *Physics of Semiconductors*. 1958, London: Infosearch.
17. Slack, D.T.M.a.G.A., *High Thermal Conductivity Materials*, ed. S.S.a.J. Goela. 2005, New York: Springer.
18. Testing, A.S.f. and Materials, *ASTM E562-01: Standard Test Method for Determining Volume Fraction by Systematic Manual Point Count*. 2002: ASTM.
19. Toby, B.H., *R factors in Rietveld analysis: How good is good enough?* Powder Diffraction, 2012. **21**(1): p. 67-70.
20. Martinez, A., D. Bellon, and L. Reina, *Quantitative phase analysis from powder diffraction using de Rietveld method in hydrogen storage alloys based on TiCr.* Journal of Physics: Conference Series, 2016. **743**(1): p. 012013.
21. Witz, G., V. Shklover, W. Steurer, S. Bachegowda, and H.-P. Bossmann, *Phase Evolution in Yttria-Stabilized Zirconia Thermal Barrier Coatings Studied by Rietveld Refinement of X-Ray Powder Diffraction Patterns.* Journal of the American Ceramic Society, 2007. **90**(9): p. 2935-2940.
22. Cullity, B.D.a.S.R.S., *Elements Of X Ray Diffraction*. 3rd ed. NATURAL SCIENCES, Physics, Physical nature of matter. 2014, U.S.A.: Addison-Wesley Publishing Company, Inc.

23. A. Monshi, M.F.a.M.M., *Modified Scherrer Equation to Estimate More Accurately Nano-Crystallite Size Using XRD.* World Journal of Nano-Science and Engineering. **2**(3): p. 154-160.
24. Chiu, C.-n., C.-m. Hsu, S.-w. Chen, and H.-j. Wu, *Phase Equilibria of the Sn-Bi-Te Ternary System.* Journal of Electronic Materials, 2012. **41**(1): p. 22-31.
25. Tamor, M.A., H. Holloway, R.M. Ager, C.A. Gierczak, and R.O. Carter, *Bismuth-doped tin telluride.* Journal of Applied Physics, 1987. **61**(3): p. 1094-1098.
26. Reza Abbaschian, L.A., Robert E. Reed-Hill, *Physical Metallurgy Principles*. 4th ed. 2009. 500-519.

CHAPTER 4

PROCESS DEPENDENT MICROSTRUCTURE of SnTe - Bi_2Te_3 SYSTEM

4.1 Introduction

The thermoelectric properties of some compositions in the pseudo-binary region of Bi_2Te_3-SnTe have been reported [1-3]. To the best of the author, these reports do not include the compositions in the regions where Bi_2Te_3 is soluble in SnTe and on the opposite side where SnTe is soluble in Bi_2Te_3.

On the other hand, there is limited information on the nature of the microstructure of the compositions in this region. This research focuses on determining the microstructure of some compositions by varying the processing method and providing information on the presence of the potential thermoelectric material. Compositions in the Bi_2Te_3 solubility limit region, according to the phase diagram of [4], are considered for this work. Two different processing roughs were taken for this experiment. The difference is in the cooling process of the melted alloy. One group of samples were cooled by ice water quenching, while the other group of samples was cooled by furnace cooling system.

It is found that the system of SnTe containing 45 to 100 mole % Bi_2Te_3 forms different solid solutions [1]. Unlike the maximum solubility of Bi_2Te_3 founded by [4], which was about 20 mole %, the report of [1] describes that the maximum solubility is about 5 mole %. The added Bi_2Te_3 changes the thermoelectric property of SnTe. This may be either by creating defects [5, 6] or by changing the electronic band structure of the system. The former includes precipitates, point

defects, and alloying effects. The latter may be due to the changing lattice constant of SnTe phase, specifically the primary α-phase, which contains soluble Bi_2Te_3. Such kind of microstructural engineering may result in the finding of thermoelectrically efficient materials since the different microstructures can affect the phonon propagation and since it is also possible to create unique electronic property at the phase and grain boundaries.

4.2 Experiment

4.2.1 Synthesis

The samples for this experiment were synthesized using the same instruments and reagents as it was used for the experiment discussed in chapter 3. The stoichiometric amount of reagents were used to prepare SnTe and Bi_2Te_3. Each of these compounds was prepared by melting the reagents, contained in the sealed quartz tube, at 900 ℃ which is high enough to homogenize the melted liquid solution and low enough to prevent evaporation of Te inside the quartz tube that will cause lack of homogenization. The sealed samples were kept in the box furnace, and the temperature reached 900 ℃ in 4 hrs. The melted liquid was held at 900 ℃ for 2 hrs. while frequently shaking it to homogenize it thoroughly. Both of these binary compounds were quenched in ice water. It is the mixture of these binary compounds that has been melted to form the pseudo-binary compound.

Sample Name	Nominal Composition, mole %	
	SnTe	Bi_2Te_3
SBT1, SBT11	97.5	2.5
SBT2, SBT22	90	10
SBT3, SBT33	82.5	17.5

Table 4.1: Composition of the samples (a), and the corresponding phase diagram (b).

This experiment was different, from what has been done in chapter 3, concerning composition and processing. The ingot was prepared from SnTe and Bi_2Te_3, rather than preparing it directly from the reagents. Accordingly, the two compounds were prepared by furnace melting, and then ice water quenching. A stoichiometric amount of three pairs of samples with three different compositions were taken to study the two different cooling processes, and three different compositions were taken to study each of the cooling procedures.

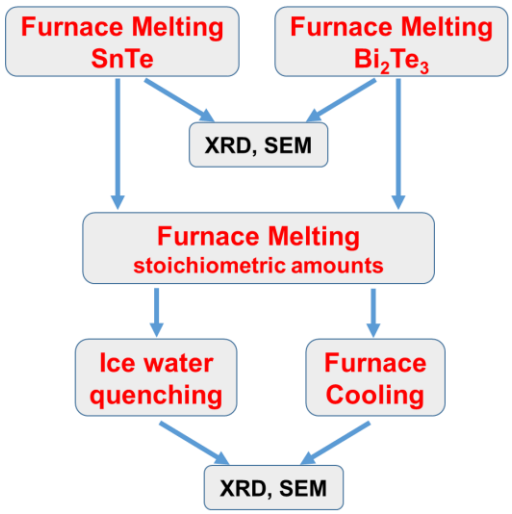

Figure 4.1: Flow chart of the experimental procedure.

4.2.2 Characterization

XRD and EPMA characterized both the binary and the pseudo-binary samples. The former characterization aims at proving the proper formation of the binary compounds, SnTe and Bi_2Te_3, whereas the latter was targeted at finding the phases formed, the solubility of Bi_2Te_3, the crystal structure of the compounds and other related properties. EPMA was used to conduct point analysis by WDS, elemental mapping and line analysis. XRD was used to identify the phases present in the

sample. Since most of the samples contain more than two phases, and hence complex XRD pattern, the Rietveld analysis is not included for this case.

4.3 Result

This experiment showed that the region studied in this chapter is more complicated. It contains several complex intermetallic compounds. The samples studied in this experiment have three phases: α-phase, $SnBi_2Te_4$ phase, and $Sn_3Bi_4Te_9$ phase. Here, the α-phase represents the SnTe phase that contains soluble Bi_2Te_3. The XRD result implies that the α-phase and $SnBi_2Te_4$ phase have Fm-3m and R-3m space groups, which correspond to cubic and rhombohedral crystal structures, respectively. To the best of this work, the third phase, $Sn_3Bi_4Te_9$, is not reported before and hence its crystal structure and space group are not available in freely available databases.

Some of the XRD peaks left, from the two well-known phases, fit with the peaks of $Sn_3Bi_4Te_9$ phase. However, still, it is not all peaks that are fitting with peaks of this compound, as it is reported by Chiu et al. [7]. There are some peaks which do not fit with α-phase, $SnBi_2Te_4$ phase or $Sn_3Bi_4Te_9$. Perhaps those peaks may fit with that of $Sn_3Bi_4Te_9$ phase if it is possible to find its XRD pattern. This may need to find the XRD pattern of the $Sn_3Bi_4Te_9$ phase, which is the stoichiometry founded by WDS analysis.

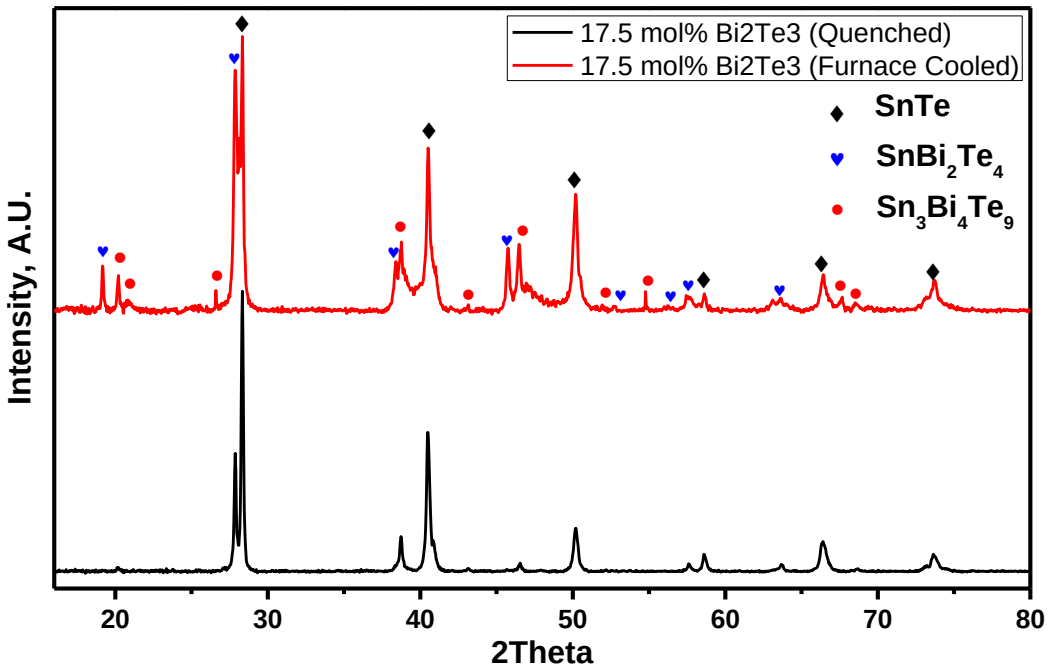

Figure 4.2: XRD pattern of the phases found for a pair of SnTe – 17.5 mole % Bi_2Te_3 systems.

The furnace cooled samples have some pattern of microstructures that looks like a group of parallel lines making some angle with another group of parallel lines. The lines seem some twin boundary observed under HRTEM. For the ease of description let them be named twin-like microstructures. Though, this may be miss leading since it is not possible to see twin boundaries by the electron microscopes used for this experiment. The angle of the twin-like boundaries changes with the change in composition. For 10 mole % Bi_2Te_3 almost all of the twin boundaries form 54 to 60 degree. However, this is changed for SBT3, which has many different angles of twin-like phase boundaries, both between similar phases and different phases. The intermediate composition may also have other different angles. This gives the opportunity to choose the necessary composition which will give better thermoelectric property or other related applications, as reported by Kim et al. [8].

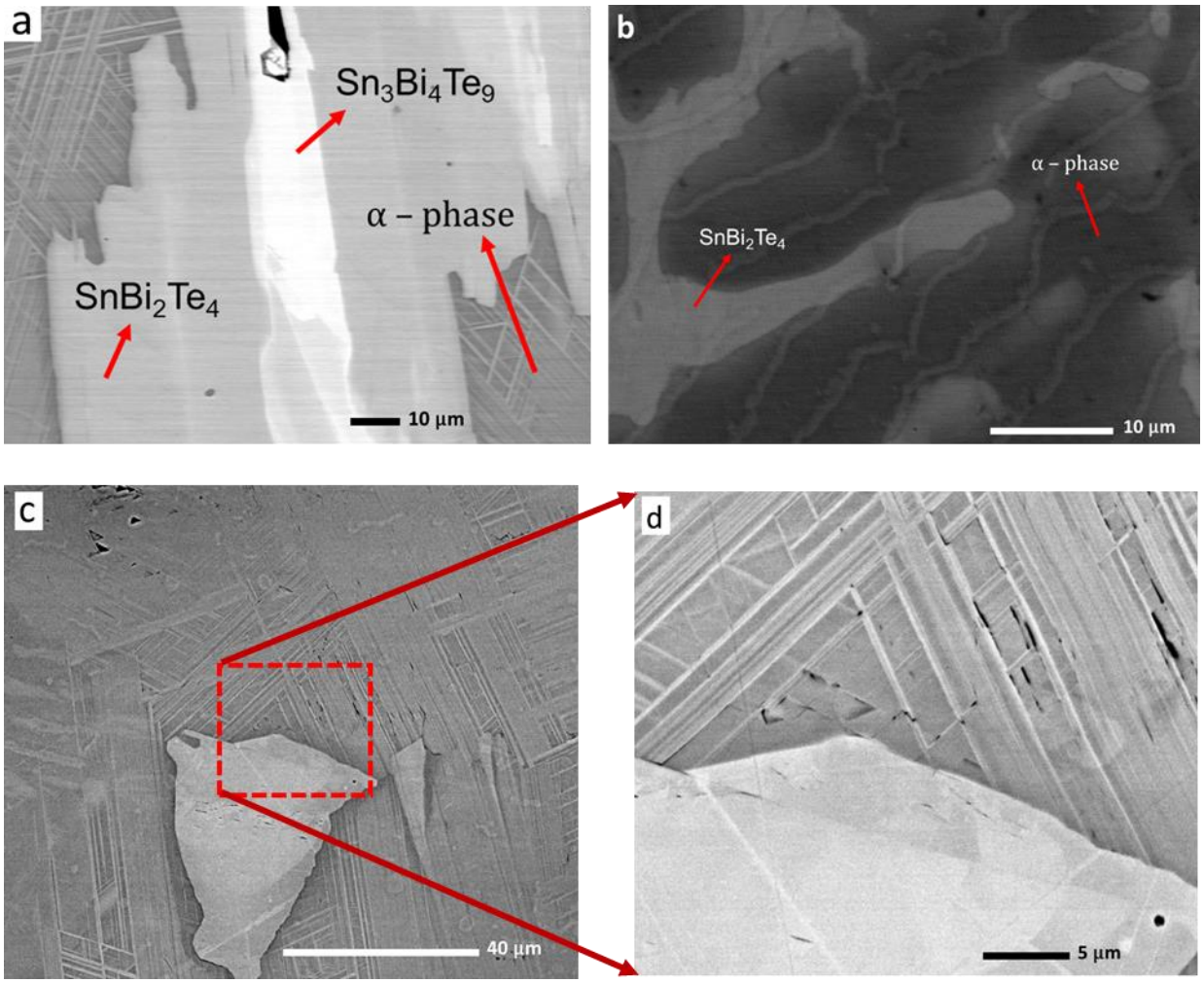

Figure 4.3: (a) and (b) shows furnace cooled and ice water quenched microstructure of SnTe – 17.5 mole % Bi_2Te_3, (c) microstructure of SnTe – 10 mole % Bi_2Te_3, (d) shows the twin-like microstructure observed in (c). The name "twin-like" is given for the sake of communication, since it has not been identified this experiment.

There was a significant difference between the detection of EDS and WDS. This may be one reason for the stoichiometric loss of Bi in the overall EDS analysis, which is about 2 mole and comparable to one granule of Bi. Since the point analysis by WDS high accuracy for the two phases, α-phase and $SnBi_2Te_4$ phase, the compositions of the three phases were taken as it was found from EPMA. The images of those phases show that they hay gray, bright, and brighter appearance. The

concentration of Bi increases with the brightness of the phases, while that of Sn decreases. Even some of the changes of Bi concentration is smaller than that the change in the concentration of Sn. This may be helpful in understanding of the working principle (detection mechanism), of the microscopy, i.e. smaller change in high atomic number elements is more influential than significant change in small atomic number element, so that more backscattered electrons are generated with smaller increase of large atomic number elements, which make the latter phases bright and/or brighter.

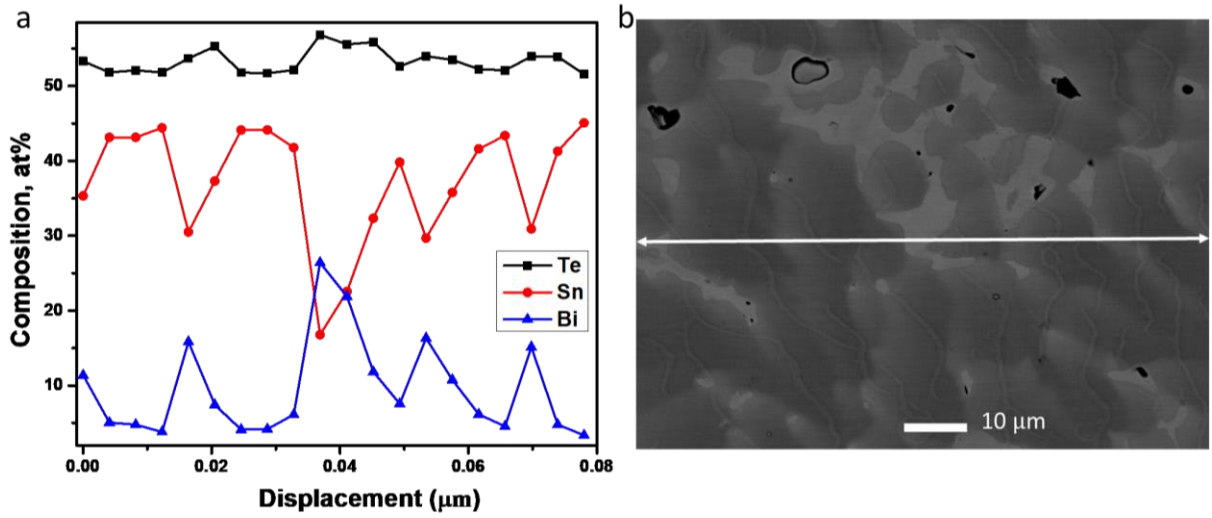

Figure 4.4: A plot of composition obtained by line analysis of the SnTe - 10 at% Bi (a), and the corresponding image (b).

4.4 Discussion

Once Bi_2Te_3 is formed to add it with the appropriate stoichiometry of SnTe, to form Bi dissolved in SnTe, either along SnTe to BiTe, or SnTe to Bi directions, in the ternary phase diagram. However, this kind of approach needs to clarify the reason why it enables the increase in Bi solubility, may be either from the perspective of the energy of solution formation of Bi or Bi_2Te_3 into SnTe, or the ease of crystal structure transformation of Bi_2Te_3. In fact, the XRD peaks of

SBT2 and SBT3, doesn't show significant shift (to the left) corresponding to the increased solubility of Bi (or Bi_2Te_3) into SnTe to form the α-phase, at least similar to Zhiwei et al. Therefore there is high probability that the Bi detected in the α-phase to be Bi precipitate, rather than Bi dissolved in SnTe. Since the size of the electron beam is 1 to 2 microns, the WDS point analysis can detect SnTe crystallite and Bi precipitate altogether. This also may be the reason why some part of the α-phase is a little brighter than some the other part. Such possibilities should be checked under HRTEM. If it is found to be the existence of Bi precipitate that is detected in the α-phase, it is also advantageous to increase the number of precipitates and the corresponding effect. Besides, if it is Bi dissolved in SnTe crystal lattice, it will be unusual nature or creation of some vacancy that keeps the change in crystal structure negligible.

α-phase contains 16.39 mol% Bi_2Te_3. This corresponds to (Sn - 13.2 at% Bi, 52.8 at% Te). Since the XRD shows that SnTe peaks are dominant, it is possible to say that about 13.2 at% Bi is dissolved in SnTe as $Sn_{1-x}Bi_xTe$ to form this phase. According to Zhou et al. [9], this phase must show a peak shift to the left, which corresponds to the increase in lattice constant of the SnTe rock salt structure. The observed peak shifts of SBT2 are to the right, indicating decreasing of lattice constant. This may be some unusual nature, together with similar phenomenon observed in the low solubility (less than 1 at %) of Bi in SnTe. Perhaps this will be solved by analyzing under HRTEM, which also will be helpful to identify the nature of the twin-like boundaries formed, i.e., type of the phase boundaries.

4.5 Conclusion

Based on the WDS point analysis, the phase boundaries are formed between Bi-rich and Bi poor phases. These phases are visible close to the bright phase, which has some brighter phase in it. The brighter the phase, the more is the concentration of Bi. Therefore the ‘twin-like' microstructures

look like emerging from the bright phase. The bright phase may have a relatively low melting point. This implies that the bright phase is formed when the molten state of low melting point phase of the sample is expelled from the growing grain of high melting point phase, during furnace cooling. This may be the reason why this ‘twin-like' phase is not observed in the quenched sample of the same composition. On the other hand quenching or fast cooling, the sample will be one method to remove or minimize the ‘twin-like' microstructure, respectively, if it played down the thermoelectric property. The following conclusions are reached from this experiment.

- ✓ It is possible to find different kind of phases within the solubility limit of Bi_2Te_3 while considering the currently available phase diagram for the solubility limit.
- ✓ It may be advantageous to study the thermoelectric property of the various phases, at least by theoretical simulation.
- ✓ The phase diagram considered during this experiment may need modification since a single phase was expected within the solubility limit.
- ✓ Both the composition and processing can result in various microstructures. This may be good to find alternatives for thermoelectric application.

4.6 References

1. al, R.A.R.e., *Phase Relations and Thermoelectric Properties of the Alloy Systems SnTe - Bi2Te3 and PbTe - Sb2Te3.* J. Electrochem. Soc., 1967 **114**(5): p. 526-529.
2. Kuropatwa, B.A. and H. Kleinke, *Thermoelectric Properties of Stoichiometric Compounds in the (SnTe)x(Bi2Te3)y System.* Zeitschrift für anorganische und allgemeine Chemie, 2012. **638**(15): p. 2640-2647.
3. Zhou, X.-S., Y. Deng, C.-W. Nan, and Y.-H. Lin, *Transport properties of SnTe–Bi2Te3 alloys.* Journal of Alloys and Compounds, 2003. **352**(1): p. 328-332.
4. Adouby, K., A. Abba Touré, G. Kra, J. Olivier-Fourcade, J.-C. Jumas, and C. Perez Vicente, *Phase diagram and local environment of Sn and Te: SnTeBi and SnTeBi2Te3 systems.* Comptes Rendus de l'Académie des Sciences - Series IIC - Chemistry, 2000. **3**(1): p. 51-58.
5. Zhao, L.D., H.J. Wu, S.Q. Hao, C.I. Wu, X.Y. Zhou, K. Biswas, J.Q. He, T.P. Hogan, C. Uher, C. Wolverton, V.P. Dravid, and M.G. Kanatzidis, *All-scale hierarchical thermoelectrics: MgTe in PbTe facilitates valence band convergence and suppresses bipolar thermal transport for high performance.* Energy & Environmental Science, 2013. **6**(11): p. 3346-3355.
6. Medlin, D.L. and G.J. Snyder, *Interfaces in bulk thermoelectric materials: A review for Current Opinion in Colloid and Interface Science.* Current Opinion in Colloid & Interface Science, 2009. **14**(4): p. 226-235.
7. Chiu, C.-n., C.-m. Hsu, S.-w. Chen, and H.-j. Wu, *Phase Equilibria of the Sn-Bi-Te Ternary System.* Journal of Electronic Materials, 2012. **41**(1): p. 22-31.
8. Kim, K.-C., J. Lee, B.K. Kim, W.Y. Choi, H.J. Chang, S.O. Won, B. Kwon, S.K. Kim, D.-B. Hyun, H.J. Kim, H.C. Koo, J.-H. Choi, D.-I. Kim, J.-S. Kim, and S.-H. Baek, *Free-electron creation at the 60° twin boundary in Bi2Te3.* Nature Communications, 2016. **7**: p. 12449.
9. Zhou, Z., J. Yang, Q. Jiang, Y. Luo, D. Zhang, Y. Ren, X. He, and J. Xin, *Multiple effects of Bi doping in enhancing the thermoelectric properties of SnTe.* Journal of Materials Chemistry A, 2016. **4**(34): p. 13171-13175.

CHAPTER 5

SUMMARY, CONCLUSION AND FUTURE WORK

5.1 Summary and Conclusion

This thesis gave information on the nature of the systems studied in the two pseudo-binary regions. It has been found that both Bi and Bi_2Te_3 have small solubility limit in SnTe. This may be due to the difference in the crystal structure between these solutes and the solvent SnTe, in the solid solution. Both Bi and Bi_2Te_3 have rhombohedral crystal structure while that of SnTe is rock salt. The solubility of Bi was smaller than that of Bi_2Te_3. Irrespective of the cooling procedure, the SnTe-Bi system has Bi secondary phase and SnTe phase, hence similar microstructure. However, the microstructure of the SnTe-Bi_2Te_3 system was processing dependent. Therefore both the processing and composition of the system were varying the microstructure.

The microstructure of the SnTe-Bi system had varied with aging heat treatment. This results in changing the mechanical property of the system. Within the microstructure, it was observed that the continuous nature of the Bi secondary phase had been changed to small particle-like phases. This may be due to the grain growth that occurs in both Bi and SnTe phases. Despite the observed changes in the microstructure of both phases, the volume fraction of each phase remains the same, as it had been determined by Rietveld refinement and cross-checked by Systematic Manual Point Counting method. It was also observed from SB7 and SB10, figure 14, that the higher the volume fraction of the Bi phase the better the measured increase in Vickers hardness of the material.

On the other hand, the microstructure of the SnTe-Bi_2Te_3 system has different features that vary as a function of both composition and processing. It is observed that the fast cooling creates only

two phases, α-phase, and $SnBi_2Te_4$ phase. The third phase, $Sn_3Bi_4Te_9$, increases with the concentration of Bi_2Te_3 or decreases with the faster cooling rate. This phase contains a relatively higher amount of Bi or Bi_2Te_3 that may be the reason for the absence of its peaks in the powder XRD pattern of SnTe - 2.5 mole % Bi_2Te_3.

The thermoelectric properties of SnTe - Bi system give some insight about the possibility of producing good thermoelectric material in the presence of Bi secondary phase. The electrical conductivity and the electronic thermal conductivity decreases with increase in Bi concentration or increasing temperature. The increasing Seebeck coefficient with increasing temperature was dominant in the power factor; as a result, the power factor increases with temperature.

Sample	Phase Fraction	SOF at 4a	Lattice Constant, Å	Number of Parameter Refined	GOF
SnTe	-	1 Sn	6.3175(2)	13	1.49238
SB7-00	90.0(4) wt% $Te_4Sn_{3.81}Bi_{0.18}$	0.04(3)Bi, 0.95(3)Sn	6.3208(2)	23	1.29379
SB7-05	88.4(3) wt% Te4Sn3.49Bi0.51	0.13(2)Bi, 0.87(2)Sn	6.3229(2)	23	1.70931
SB7-10	90.6(2)wt% Te4Sn3.34Bi0.66	0.17(2)Bi, 0.83(2)Sn	6.3223(1)	24	1.33138
SB7-15	90.3(3) wt% Te4Sn3.42Bi0.58	0.15(3)Bi, 0.85(3)Sn	6.3226(2)	25	1.12587
SB7-20	91.0(3)wt% Te4Sn3.55Bi0.45	0.11(2)Bi, 0.89(2)Sn	6.3232(2)	24	1.2503
SB10-00	85.1(3) wt% Te4Sn3.24Bi0.76	0.19(3)Bi, 0.81(3)Sn	6.3221(2)	23	1.36172
SB10-05	87.3(2) wt% Te4Sn3.6Bi0.4	0.10(2)Bi, 0.90(2)Sn	6.3226(1)	21	1.26729
SB10-10	86.0(3)wt% Te4Sn3.58Bi0.42	0.10(2)Bi, 0.90(2)Sn	6.3217(2)	23	1.29298
SB10-15	88.6(14)wt% Te4Sn3.98Bi0.02	0.01(2)Bi, 0.99(2)Sn	6.3221(1)	24	1.00635
SB10-20	85.6(9) wt% Te4Sn3.38Bi0.62	0.16(3)Bi, 0.84(3)Sn	6.3230(2)	25	1.11174

Table 5.1: Summary of the Rietveld refinement. The number separated by '-' from the sample name indicates the time taken (in hrs) for aging.

5.2 Future Work

The lesson that was obtained in this work was both conducting experiment to analyses the two pseudo-binary systems and getting practical experience on how to experiment in a laboratory. Accordingly, the experience that has been developed in this work will be used for developing other experiments and for studying different systems from a different perspective. The overall approach of this thesis implies that it is preferable to include simulation and theoretical calculations both to save resource for practical experiment and to understand the different phenomenon from the atomistic point of view. This includes the following points:

- ✓ Finding thermoelectric contact material is one of the challenges in the current state of the art. Based on some observations during this experiment, it is believed that it is possible to find thermoelectric contact material using a directional solidification process.
- ✓ Optimizing the thermoelectric and thermodynamic nature of the phase and grain boundaries of the systems studied in this work.
- ✓ Quantum mechanical simulation and numerical calculation will be the first step of the future work, in order to optimize the systems and understand the atomistic and particle nature of the material.
- ✓ Looking for different dopants that can modify the SnTe system and including all scale hierarchical process.